ISSN 2409-5613 (print)
ISSN 2411-1414 (online)

Chimica Techno Acta

2017. Vol. 4. N 3

cta.urfu.ru

Founded by Ural Federal University named after the first President of Russia B. N. Yeltsin
19, Mira St., Ekaterinburg, 620002, Russia

Учредитель – Уральский федеральный университет имени первого Президента России Б. Н. Ельцина
620002, Россия, Екатеринбург, ул. Мира, 19

Chimica Techno Acta

2017 | Vol. 4 | № 3

Scientific and Technical Journal
Established in 2014
Published four times per year

Chimica Techno Acta

Chimica Techno Acta

2017 | Vol. 4 | № 3

Научно-технический журнал
Журнал основан в 2014 г.
Выходит четыре раза в год

Chimica Techno Acta

Graphical Abstracts

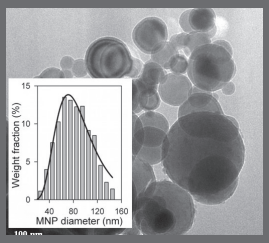

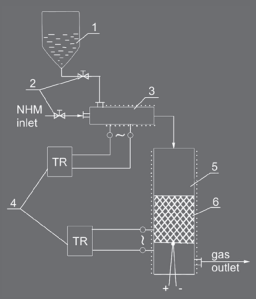

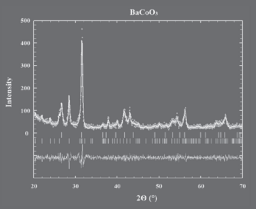

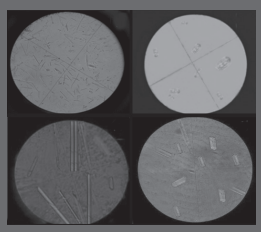

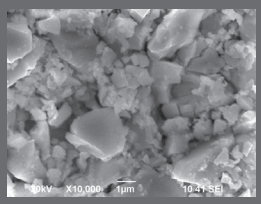

CONTENTS/СОДЕРЖАНИЕ

Shankar A., Safronov A., Beketov I.
Chimica Techno Acta. 2017. Vol. 4, No. 3. P. 158–166.
ISSN 2409–5613

DOI: 10.15826/chimtech/2017.4.3.01

Ajay Shankar[1], Alexander Safronov[2,3], Igor Beketov[3]

[1]Indira Gandhi National Tribal University,
Amarkantak, Madhya Pradesh, 484886, India
e-mail: ajayshankar0@gmail.com
[2]Ural Federal University,
19 Mira St., Ekaterinburg, 620002, Russian Federation
e-mail: safronov@iep.uran.ru
[3]Institute of Electrophysics UB RAS,
106 Amundsen St., Ekaterinburg, 620016, Russian Federation
e-mail: beketov@iep.uran.ru

Encapsulation of metallic iron magnetic nanoparticles by polyacrylamide in water suspensions

Theoretical consideration of the factors of the stability of metallic iron magnetic nanoparticles (MNPs) in water suspensions was done using extended DLVO (Derjaguin-Landau-Verwey-Overbeek) approach based on the balance among Van der Waals, electrostatic, magnetic and steric interactions. Magnetic and steric interactions dominate over other in suspensions of Fe MNPs. To test the theory Fe MNPs with average diameter 84 nm were synthesized by electrical explosion of wire and encapsulated by polyacrylamide in water suspension to provide steric repulsion. It was shown that encapsulation resulted in the efficient diminishing of the aggregation of metallic iron MNPs in water.

Keywords: Iron nanoparticles; encapsulation; polyacrylamide.

Received: 28.06.2017; accepted: 24.07.2017; published: 20.10.2017.

Introduction

Magnetic nanoparticles (MNPs) are the subject of intensive research due to the special properties required for technological and biomedical applications such as magnetic fluids, catalysis, magnetic resonance imaging, data storage, and environmental remediation [1–3]. In these applications magnetic material is to be dispersed in a solid phase giving a composite material, or in a liquid giving a ferrofluid or a suspension. Among others iron-based MNPs attract special attention due to their relatively low cost and comparatively low toxicity for the living systems, which is of the major importance for the biotechnological and biomedical applications. In this respect iron oxide MNPs are mostly studied. There are a lot of different methods for their synthesis, a variety of actual and prospective applications [3], and numerous studies of their compatibility [4]. At the same time metallic iron MNPs are less studied. Meanwhile, from the viewpoint of their magnetic properties metallic iron has indisputable advantages over its oxides. Its saturation

magnetization is at least three times higher than that of magnetite. If used in magnetic sensors, actuators, contrast agents for MRS iron MNPs might provide higher sensitivity, better response, and lower detectable doses. However, there are several unresolved problems of the application of metallic iron MNPs in suspensions. The major one is strong aggregation of metallic iron MNPs.

It is known, that the aggregation of nanoparticles is thermodynamically favorable process. The surface between coexisting phases carries on excess free energy, which might be very high for the nanosystem as its specific surface is also high due to small dimensions. The aggregation of MNPs diminishes the surface of the direct contact among the phases and leads to the minimization of the free surface energy [5]. In order to overcome the thermodynamic force for the aggregation and to provide the stability of disperse systems with nanoparticles, such approaches as electrostatic or steric stabilization are used. Unfortunately, the variety of stabilizers, which proved to be successful for the stabilization of iron oxide suspensions, are not such for the suspensions of metallic iron particles in water. It is the result of the enhanced magnetic properties of iron, which dominate over other forces in colloid suspensions.

The objective of the present study was to examine the problem of the stability of magnetic iron nanoparticles from theoretical point of view and experimentally test the possibility of the stabilization of the suspension of spherical iron MNPs in water, using their encapsulation by water-soluble polymer – polyacrylamide.

Experimental

Materials

Metallic iron magnetic nanoparticles (MNP) were synthesized by the method of electric explosion of wire (EEW). The detailed description of EEW equipment designed at the Institute of Electrophysics of RAS (Ekaterinburg, Russia) is given elsewhere [6–8]. The method is based on the evaporation of a portion of metal wire by the electric high power pulse in the explosion chamber filled with the inert atmosphere. Further condensation of the expanding metal vapors resulted in the formation of spherical MNPs. The applied voltage was 30 kV and the length of the exploded portion of wire was 70 mm. The wire was continuously fed to the explosion chamber by the feeding device, the high voltage source was concurrently recharged after each explosion, and the process was repeated in the pulsed manner resulted in rapid production of MNPs (200 g/h). The reaction chamber was filled with a circulating mixture of 70 % of Ar and 30 % of N_2 providing the working gas pressure of 0.12 MPa.

Polyacrylamide (PAAm) was synthesized by the radical polymerization reaction of acrylamide (AAm) (AppliChem, Darmstadt) in 1.6 M water solution at 80 °C. Ammonium persulfate (PSA) in 5 mM concentration was used as an initiator. The reaction mixture was kept at 80 °C for 1 h. The obtained PAAm solution was then diluted with distilled water down to 5 % concentration by weight. The resulted solution was then used as a stock for the encapsulation of iron MNPs. The molar weight of PAAm determined by viscometry was M = 1.46*105 g/mol.

Methods

The powder X-ray diffraction (XRD) patterns were recorded using Bruker D8 Discover with Cu Kα radiation (λ = 1.542 Å) with graphite monochromator. The Rietveld refinement of XRD patterns were performed using Topas-3 software. The morphology of MNPs was examined using JEOL JEM2100 transmission electron microscope (TEM) operating at 200 kV. The specific surface area of MNPs was measured by the low-temperature adsorption of nitrogen (Brunauer-Emett-Teller (BET) approach) using Micromeritics TriStar3000 analyzer. The magnetic measurements were carried out using (Cryogenics Ltd. VSM) vibrating sample magnetometer (VSM) at room temperature for powder samples placed in a gelatine capsule. The magnetization values in a field of 1.8 T were designated as the saturation magnetization values (M_s). Thermal analysis was done using NETZSH STA409 thermal analyzer operated in linear heating mode from 40 to 1000 °C at 10 K/min in the air. Dynamic light scattering (DLS) and electrophoretic light scattering (ELS) measurements were performed using Brookhaven ZetaPlus particle size analyzer: 5 and 3 runs were recorded for hydrodynamic size and zeta-potential measurements, respectively.

Results and their discussion

Theory

The aggregation features of iron MNPs in water suspension can be qualitatively modeled by the extended DLVO approach. In classical DLVO theory, the attractive and repulsive interactions are modeled for van der Waals and electrostatic interactions only. In case of the magnetic colloidal dispersions where both steric and magnetic interactions are also present, they must also be taken into account. The modified approach to consider all these interactions is known as xDLVO approach [9]. This theory was elaborated to study the stability of iron MNPs in water suspension.

The van der Waals interaction energy (V_{vdW}) between MNPs with radius r at a distance s was calculated as [10]:

$$V_{vdW} = \frac{-A(r)}{6}\left[\frac{2r^2}{s(4r+s)} + \frac{2r^2}{(2r+s)^2} + \ln\left\{s\frac{(4r+s)}{(2r+s)^2}\right\}\right], \quad (1)$$

where

$$A(r) = 1.77\times10^{-19} + 1.60\times10^{-19}e^{-r/3.05} + 6.35\times10^{-20}e^{-r/10.75} + 2.05\times10^{-20}e^{-r/52.18}\ [\mathrm{J}].$$

The electrostatic repulsions under constant charge boundary condition were taken as [11]:

$$V_e = 2\pi r\varepsilon_r\varepsilon_o\psi_o^2\ln\left(1+e^{-\kappa s}\right), \quad (2)$$

where

$$\kappa = \left(\frac{k_B T\varepsilon_0\varepsilon_r}{q^2 N_A\sum z_i^2 c_i}\right)^{-1/2}.$$

Here ε_r is the relative dielectric constant of water, ε_0 is the permittivity of free space, ψ_0 is the surface potential, q is the elementary charge, z_i is the charge of simple ions, c_i is their molar concentration, N_A, k_B, and T have their usual meanings. We used the value of electrokinetic (zeta) potential of –16 mV for iron MNPs in water (by ELS) as an approximation for the surface potential.

The steric repulsion was taken into account through a hard core combined with a soft tail potential, as modeled previously under self-consistent field (SCF) theory.

This originating overall steric term for two identical stabilized MNPs was taken as [12]:

$$V_{st} = \begin{cases} \infty & \text{for } s < 0 \\ \left(\frac{r\pi^3\delta^3\sigma_p kT}{12N_p l^2}\right)\left[-\ln\left(\frac{s}{2\delta}\right) - \frac{9}{5}\left(1-\frac{s}{2\delta}\right) + \frac{1}{3}\left(1-\left(\frac{s}{2\delta}\right)^3\right) - \frac{1}{30}\left(1-\left(\frac{s}{2\delta}\right)^6\right)\right] & \text{for } 0 < s < 2\delta \\ 0 & \text{for } s > 2\delta \end{cases} \quad (3)$$

where, δ is thickness of adsorbed LPAAm layer, σ_p is surface density of adsorbed chains, N_p is number of free segments and l is the length of one free segment.

The maximum magnetic attraction energy (V_M) between MNPs was taken as [10]:

$$V_M = \frac{-8\pi\mu_o M^2 r^3}{9\left(\frac{s}{r}+2\right)} \quad (4)$$

The total energy of interaction between iron MNPs was calculated as a combination of equations (1)–(4).

$$V(s) = V_{vdW}(s) + V_e(s) + V_{st}(s) + V_M(s) \quad (5)$$

Considering contributions from different terms in equation (5) it was found out that steric (equation (3)) and magnetic (equation (4)) terms are dominating for iron MNPs. These two terms in turn strongly depend on such parameters of MNPs as the radius, the thickness of the steric protective layer, and the magnetization of particle. Fig. 1 presents the dependence of the energy of interparticle interaction at different combinations of these parameters. The parameters are taken close to that characteristic for the MNPs studied below.

It is noticeable that each curve in Fig. 1 has a minimum, which is the result of the balance among attractive magnetic force and repulsive steric interaction. It is con-

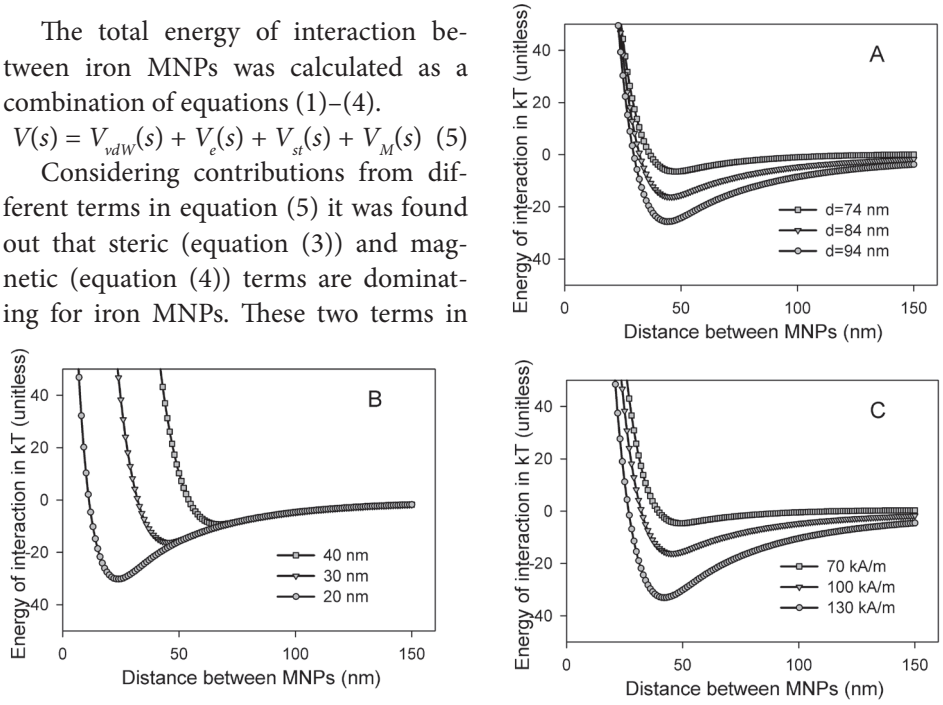

Fig. 1. Energy of interaction as a function of the distance between iron MNPs: A – The influence of the diameter of MNPs at constant thickness of steric layer (30 nm) and constant magnetization (100 kA/m); B – The influence of the thickness of steric layer of MNPs at constant diameter (84 nm) and constant magnetization (100 kA/m); C – The influence of the magnetization of MNPs at constant diameter (84 nm) and constant thickness of steric layer (30 nm)

ventionally accepted that the aggregates can be disrupted by the thermal motion if the corresponding minimum is less than 20 k_BT, as statistically only a few particles will cross barrier in this case [13]. Thus, the depth of the minimum indicates the tendency of the ensemble of MNPs to aggregation. It is obvious that the depth of the minimum increases with the increase of particle radius, with the increase in magnetization, and the diminishing of the thickness of protective layer.

Based on these results, we analyzed the possibility of de-aggregation of Fe MNPs by their encapsulation by polyacrylamide.

Characterization of metallic iron MNPs

Fig. 2 presents TEM image of metallic iron MNPs synthesized by EEW. They are spherical in shape and non-aglomerated. The spherical shape of MNPs is the result of the EEW conditions. The electrical pulse, which passes the portion of wire, provides its overheating to ca 10^4 K and complete vaporization. Then iron MNPs

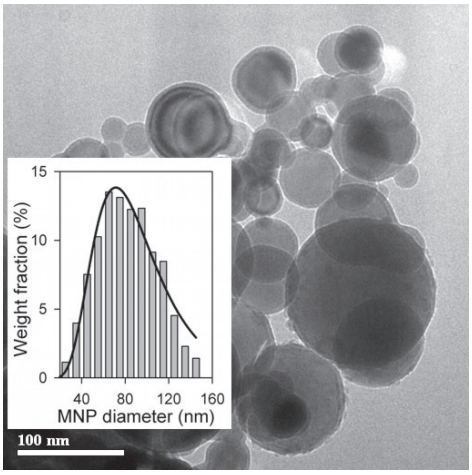

Fig. 2. TEM image of metallic iron magnetic nanoparticles synthesized by electric explosion of wire. Inset: histogram – calculation of particle weight fraction from the image analysis, line – fitting of PSD by equation (6)

are condensed in a vapor phase under the thermodynamic condition for the minimization of free energy. The sphere has a minimal surface among other possible geometrical figures with a constant volume. Hence, the obtained iron MNPs condense in a shape of spheres. The density of vaporized metal in the EEW explosion chamber is kept low by constant circulation of inert working gas; it minimizes the probability of collisions among condensing MNPs and prevents their coalescence in liquid phase. The particle size distribution (PSD) (Fig. 2, Inset), which was obtained by the graphical analysis of more than 2000 images of MNPs, fits well the following lognormal equation:

$$PSD(d) = \frac{10.70}{d} e^{-\frac{(\ln d - \ln(83.9))^2}{2*0.402^2}} \qquad (6)$$

The specific surface area of MNPs (Ssp) measured by the low-temperature adsorption of nitrogen was 9.0 m^2/g. The surface average diameter of MNPs, calculated from this value using the equation $d_s = 6/(\rho S_{sp})$ ($\rho = 7.87$ g/cm^3 being iron oxide density) was 84.7 nm. It was in a good agreement with the median diameter 83.9 nm in PSD described by Equation (6) (the latter value was used a basic level in the theoretical calculations given above).

Fig. 3 shows XRD patterns of iron particles. MNPs contain 93 % of α-Fe with a = 2.867(2) Å and coherent length 82(5) nm and 7 % of cubic phase of γ-Fe with a = 3.591(3) Å and coherent length 27(2) nm. The coherent length of α-Fe phase perfectly correlates with the average diameter of Fe MNPs obtained both by the analysis of TEM images and by the calculation based on BET sorption results. It means that each singular MNP is a monocrystalline particle. The coherent length of γ-Fe phase is much lower. Most

likely it means that γ-Fe phase predominantly corresponds to the smallest MNPs in the ensemble.

Magnetic hysteresis loops of iron MNPs (see Fig. 4) are typical for the magnetically soft materials. The low field behavior (inset in Fig. 4) reveals the existence of magnetic hysteresis and coercivity.

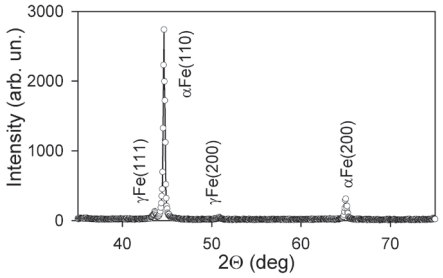

Fig. 3. XRD diffractogram of iron MNPs synthesized by EEW

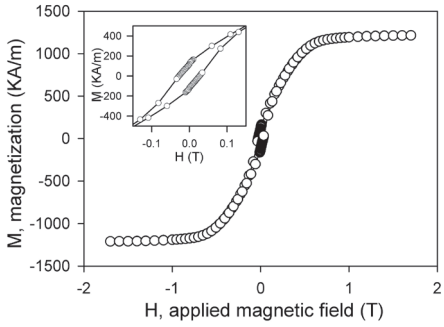

Fig. 4. Magnetic hysteresis loop of Fe MNPs at 25 °C. Inset – enlarged view of hysteresis loop in low fields

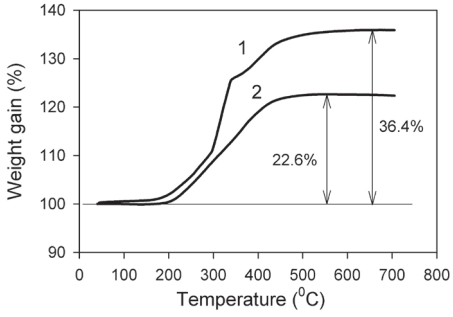

Fig. 5. Thermograms of the heating of pristine MNPs (1) and encapsulated MNPs (2) in the air

It can be understood taking into account that although in the ensemble of spherical iron MNPs with average diameter of about 82 nm the majority of them are in multidomain state, one cannot exclude the presence of a small fraction of single domain MNPs contributing to non-zero coercivity. The value of the saturation magnetization in bulk state for pure iron is M_s = 1710 (kA/m) [14] for room temperature. The obtained value for M_s for MNPs is about 30 % lower. Most likely this difference stems from two reasons. First, there is a thin oxide layer on the surface of iron MNPs, which appear inevitably if the active surface of MNPs is exposed to the air. The layer 5 nm in thickness can not be detected by XRD but as the magnetization of iron oxide is lower, it certainly contributes to the diminishing of M_s values for MNPs. Another possibility is the disturbance of the crystalline structure of iron in several layers adjacent to the surface of a spherical nanoparticle. These layers are not contributing to the ferromagnetic response due to the insufficient number of the nearest neighbours [15]. Both processes are contributing to M_s reduction but it is difficult to make more precise analysis first of all due to the existence of the MNPs size distribution.

Encapsulation of Fe MNPs by PAAm

Encapsulation of iron MNPs was performed by grinding in an agate mortar with 5 % water solution of PAAm at 25 °C. Then the slurry was diluted by the excess of distilled water. The supernatant was decanted and the precipitant was washed several times by distilled water; after that it was collected and tested.

The total amount of PAAm, which adsorbed onto Fe MNPs was determined by TG/DSC thermal analysis. Fig. 5 presents

the thermograms for the initial Fe MNPs and MNPs encapsulated by PAAm.

Both pristine MNPs and encapsulated MNPs exhibit weight gain (Fig. 5A) in the process of heating. It is the result of the oxidation of iron by the atmospheric oxygen. There is clear difference in the total weight gain of these two samples. It stems from the decomposition of PAAm deposit on the surface of MNPs, which effectively decreases the weight gain. The difference of the weight gain is ca 14 %. This value corresponds to the PAAm deposit on the surface of MNPs. The thickness of this layer can be estimated using the residual amount of LPAAm on the surface of MNPs determined by thermal analysis. Corresponding conversion into volume fraction taking into account the difference in densities of PAAm and Fe core gives 40 % of polymer. The calculation of the thickness of a layer at the surface of the spherical particle with the diameter 90 nm gives ca 8 nm for the layer. Meanwhile, this value corresponds to the dry layer of polymer on the surface. If the MNPs are dispersed in water the polymeric layer swells and its thickness increases. If we assume that the conformation of PAAm macromolecules in the layer is a random Gaussian coil, the volume fraction of a polymer in a coil is given by the following relation:

$$\varphi_G = \frac{6^{3/2}}{8\sqrt{N}} \qquad (7)$$

N is the number of monomeric segments in the chain. The number of Kuhn segments for the molecular weight of PAAm (143.6 kDa) is N = 500, which in turn gives $\varphi_G = 0.08$. It is a reasonable estimation for the volume fraction of PAAm in a swollen Gaussian coil. Thus, in water the volume of PAAm layer increases by a factor of 1/0.08 = 12.5. Then, the thickness of a layer increases up to ca. 30 nm. (This value was used as a basic level in the theoretical calculations given above)

Fig. 6 presents multimodal distribution of particles/aggregates in water suspension of iron MNPs encapsulated by PAAm. PSD of iron MNPs in water suspension comprises two peaks. The first one is positioned at 160–200 nm. This peak most likely corresponds to individual Fe MNPs in suspension. The estimation of the characteristic dimensions of encapsulated particle, which comprises 84 nm Fe core and 30 nm PAAm steric protective layer on the surface gives ca 144 nm for the diameter. It is rather close to the position of the first peak at the PSD plot. The second mode is positioned at ca 1000 nm. This peal obviously stans for the aggregates of MNPs. The relative number fractions of these two peals are 90 % for the individual MNPs and 10 % for large aggregates. It means that individual MNPs dominate over aggregates in iron MNPs suspension. Qualitatively, this result is in agreement with the conclusions made based on the theoretical consideration, which favoured the possibility of de-aggregation of iron MNPs if sterically stabilized by protective layers.

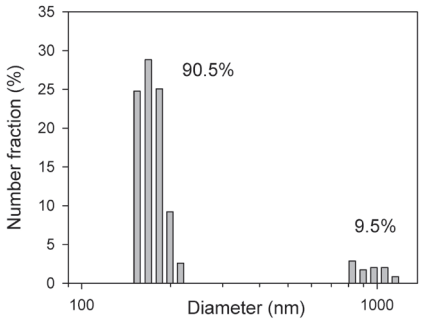

Fig. 6. Multimodal PSD of iron MNPs in water suspension by DLS

However, full de-aggregation was not achieved. The fraction of aggregates is still substantial. Most likely it is due to high polydispersity of MNPs. As it was shown in Theory section the energy of interaction among MNPs strongly depends on their radius. If the ensemble of MNPs is polydisperse, then there is a large fraction of particles with enhanced interaction. This fraction obviously provides aggregation which can not be prevented by 30 nm PAAm layers.

Conclusions

The factors of aggregation of Fe magnetic nanoparticles (mean diameter 84 nm) in water suspension were analyzed using extended DLVO (Derjaguin-Landau-Verwey-Overbeek) approach. It is based on the balance among Van der Waals, electrostatic, magnetic and steric interactions. It was shown that attractive magnetic and repulsive steric interactions dominate over other in suspensions of Fe MNPs. As a result of their superposing the dependence of the energy of interaction between MNPs exhibits minimum, which corresponds to the formation of aggregates of MNPs. If the depth of the minimum is less than 20 kT, the aggregates can be disrupted by the thermal motion. The depth of the minimum is very sensitive to the size of MNP, to its magnetization, and to the thickness of the layer on its surface. It was shown that for Fe MNPs 84 nm in diameter and magnetization 100 kA/m the threshold of the stability corresponds to the protective layer 30 nm. To test the theory Fe MNPs synthesized by electrical explosion of wire were encapsulated by polyacrylamide in water suspension to provide steric repulsion. It was shown that the fraction of PAAm in the protective layer is around 14 % and it resulted in the efficient diminishing of the aggregation of metallic iron MNPs in water.

Acknowledgement

Authors thank Dr. K. Balymov for performing the magnetic characterization of MNPs, Dr. A. I. Medvedev and Dr. A. M. Murzakayev for special support.

References

1. Huber DL. Synthesis, Properties, and Applications of Iron Nanoparticles. *Small.* 2005;1(5):482-501. DOI:10.1002/smll.200500006.
2. Llandro J, Palfreyman JJ, Ionescu A, Barnes CHW. Magnetic biosensor technologies for medical applications: a review. *Med Biol Eng Comput.* 2010;48(10):977–98. DOI:10.1007/s11517-010-0649-3.
3. Lu AH, Salabas EL, Schuth F. Magnetic nanoparticles: synthesis, protection, functionalization, and application. *Angew Chem Int Ed Engl.* 2007;46(8):1222–44. DOI:10.1002/anie.200602866.
4. Liu G, Gao J, Ai H, Chen X. Applications and Potential Toxicity of Magnetic Iron Oxide Nanoparticles. *Small.* 2013;9(9–10):1533–45. DOI:10.1002/smll.201201531
5. Hiemenz PC, Rajagopalan R. Principles of Colloid and Surface Chemistry. New York: Marcel Dekker, 1997. 499 p. ISBN9780824793975.

6. Kurlyandskaya GV, Bhagat SM, Safronov AP, Beketov IV, Larrañaga A. Spherical magnetic nanoparticles fabricated by electric explosion of wire. *AIP Adv.* 2011;1:042122. DOI:10.1063/1.3657510.
7. Beketov IV, Safronov AP, Medvedev AI, Alonso J, Kurlyandskaya GV, Bhagat SM. Iron oxide nanoparticles fabricated by electric explosion of wire: focus on magnetic nanofluids. *AIP Adv*. 2012;2:022154. DOI:10.1063/1.4730405.
8. Safronov AP, Kurlyandskaya GV, Chlenova AA, Kuznetsov MV, Bazhin DN, Beketov IV, Sanchez-Ilarduya MB, Martinez-Amesti A. Carbon Deposition from Aromatic Solvents onto Active Intact 3d Metal Surface at Ambient Conditions. *Langmuir*. 2014;30(11):3243–53. DOI:10.1021/la4049709.
9. Diguet G, Beaugnon E, Cavaillé JY. Shape Effect in the Magnetostriction of Ferromagnetic Composite. *J Magn Magn Mater*. 2010;322(21):3337–41. DOI:10.1016/j.jmmm.2010.06.020.
10. Sanchez-Dominguez M, Rodriguez-Abreu C. Nanocolloids: A Meeting Point for Scientists and Technologists. Netherlands: Elsevier, 2016. ISBN978-0-12-801578-0.
11. Walker DA, Kowalczyk B, de la Cruz MO, Grzybowski BA. Electrostatics at the nanoscale. *Nanoscale*. 2011;3(4):1316–44. Doi:10.1039/C0NR00698J.
12. Lim JK, Majetich SA, Tilton RD. Stabilization of Superparamagnetic Iron Oxide Core–Gold Shell Nanoparticles in High Ionic Strength Media. *Langmuir*. 2009;25(23):13384–93. DOI:10.1021/la9019734.
13. Rosensweig RE. Ferrohydrodynamics. USA: Dover books on physics, 2014. 344 p. ISBN9780486678344.
14. O'Handley RC. Modern Magnetic Materials. New York: John Wiley & Sons, 1972. 740 p. ISBN978-0471155669.
15. Jun YW, Seo JW, Cheon J. Nanoscaling Laws of Magnetic Nanoparticles and Their Applicabilities in Biomedical Sciences. *Acc Chem Res*. 2008;41(2):179–89. DOI:10.1021/ar700121f.

Cite this article as:
Shankar A, Safronov A, Beketov I. Encapsulation of metallic iron magnetic nanoparticles by polyacrylamide in water suspensions. *Chimica Techno Acta*. 2017;4(3):158–66. DOI:10.15826/chimtech/2017.4.3.01.

DOI: 10.15826/chimtech/2017.4.3.02
УДК 66.092.57 (546.263.3-31+546.264-31)

Efremov V. N., Golosman E. Z., Kashinskaya A. V.,
Mugenov T. I., Zolotareva V. E., Polivanov B. I., Polushin A. P.
Chimica Techno Acta. 2017. Vol. 4, No. 3. P. 167–182.
ISSN 2409–5613

V. N. Efremov[1], E. Z. Golosman[1], A. V. Kashinskaya[1], T. I. Mugenov[2], V. E. Zolotareva[2], B. I. Polivanov[1], A. P. Polushin[3]

[1]OOO «NIAP-Katalizator»
10 Svyazi st., Novomoskovsk, Tul'skaya obl., 301660, Russia
[2]Novomoskovsk Institute (branch) of the
Dmitry Mendeleev University of Chemical Technology of Russia
8 Druzhby st., Novomoskovsk, Tul'skaya obl., 301665, Russia
[3]JSC «Novomoskovsk joint stock company AZOT»
Svyazi st., Novomoskovsk, Tul'skaya obl., 301660, Russia
e-mail: evgolosman.niap@yandex.ru

Resistance of industrial nickel-containing methanation catalysts to the poisoning by organic carbon dioxide absorbents

We report the results of studies on the influences of the organic carbon dioxide absorbent – aqueous solution of activated methyldiethanolamine (MDEA) – on the physico-chemical and mechanical characteristics of nickel-alumina catalyst NIAP-07-01 (NKM-1) and cement-containing catalysts NIAP-07-07 (NKM-7), Meth-134 and Meth-135 for the hydrogenation of carbon oxide (methanation). It is established that for the nickel-alumina and nickel-cement-containing catalysts subjected to activated methyldiethanolamine (MDEA) it's possible to restore their strength and catalytic properties.

In order to increase the time of operation of the methanator it is recommended to apply a new Nickel cement-containing catalyst NIAP-07-07 (NKM-7), which can be produced as tablets, rings or extrudates.

Keywords: nickel-containing catalyst; calcium aluminate; methantion; solution of methyldiethanolamine; hydrogenation; carbon oxides; catalytic activity; mechanical strength.

Received: 16.06.2017; accepted: 06.09.2017; published: 20.10.2017.

В. Н. Ефремов[1], Е. З. Голосман[1], А. В. Кашинская[1], Т. И. Мугенов[2], В. Е. Золотарева[2], Б. И. Поливанов[1], А. П. Полушин[3]

[1]ООО «НИАП-Катализатор»
ул. Связи 10, г. Новомосковск, Тульская обл., 301660, Россия
[2]Новомосковский институт (филиал) Российского химико-технологического университета имени Д. И. Менделеева
ул. Дружбы 8, г. Новомосковск, Тульская обл., 301665, Россия
[3]АО «Новомосковская акционерная компания «АЗОТ»
ул. Связи, г. Новомосковск, Тульская обл., 301660, Россия
e-mail: evgolosman.niap@yandex.ru

Устойчивость никелевых промышленных катализаторов метанирования к воздействию органических абсорбентов удаления диоксида углерода из синтез-газа

Приведены результаты исследований воздействия органического абсорбента в виде водного раствора активированного метилдиэтаноламина (МДЭА), являющегося абсорбентом диоксида углерода при его удалении из азото-водородной смеси, на физико-химические и физико-механические характеристики никельалюминиевого марки НИАП-07-01 (НКМ-1) и цементсодержащих марки НИАП-07-07 (НКМ-7), Meth-134 и Meth-135 катализаторов гидрирования оксидов углерода (метанирования). Установлено, что никельалюминиевые и никельцементсодержащие катализаторы, подвергнутые воздействию активированного метилдиэтаноламина (МДЭА), восстанавливают свои прочностные и каталитические свойства.

Для увеличения времени эксплуатации метанатора рекомендуется применять новый никелевый цементсодержащий катализатор марки НИАП-07-07 (НКМ-7), который может изготавливаться в виде таблеток, колец или экструдатов.

Ключевые слова: никелевый катализатор; алюминат кальция; метанирование; раствор метилдиэтаноламина; гидрирование; оксиды углерода; каталитическая активность; механическая прочность.

Поступило: 16.06.2017; принято: 06.09.2017; опубликовано: 20.10.2017.

Introduction

In the USSR, Russia and CIS the most commonly used catalysts of the hydrogenation of carbon oxide (methanation) are those developed by «NIAP-Katalizator»: nickel-aluminum catalyst NIAP-07-01 (NKM-1), nickel cement-containing ones – NIAP-07-02, NIAP-07-03 (NKM-4A), and nickel-chromia-alumina-

containing TO-2M [1–5]. These catalysts are manufactured according to TU2178-003-00209510-2006 by the «NIAP-Katalizator» factory, and until recently they were also produced by Dorogobuzhskiy catalyst factory and Severo-Donetsk catalyst production plant. As for now, these catalysts are produced solely by «NIAP-Katalizator». Their planned service life is usually about 15–16 years, while the actual service life amounted to 22–24 years [6] on the three JSC «AZOT» factories (Nevinnomyssk, Voronezh, Grodno).

Note that there are some imported catalysts of methanation supplied by «Haldor Topsoe», «Johnson Matthey» and «CLARIANT» (Sud-Chemie). The «NIAP-Katalizator»-made catalysts are being produced as tablets or rings in accordance with the technical requirements of TU2178-003-00209510-2006 (catalysts of methanation). For the Russian market the imported catalysts are also available as tablets, and in addition – as extrudates and beads.

The methanation catalysts must have high activity in the hydrogenation process, leaving no more than 5–10 ppm of residual CO after the methanation of 0.3–0.7 % CO and 0.02–0.1 % CO_2 mixture. They have to possess increased thermal stability without reducing their catalytic activity (overheating up to 550-650 °C can occur in cases of increasing the CO content in the source gas to more than 1 %), high mechanical strength and low gas flow resistance.

The quality of the methanation catalysts is largely determined by their support. In the domestic and imported industrial methanation catalysts various supports are used, for example, γ-Al_2O_3, calcium aluminates, compounds of CaO-MgO, γ-Al_2O_3-Cr_2O_3, γ-Al_2O_3, calcium aluminate, boehmite (AlOOH) – γ-Al_2O_3 [7–9].

The content of active component (NiO) in the industrial methanation catalysts varies in the range of 25.0 to 45.0 wt. %. Catalysts NIAP-07-02, NIAP-07-03, and KATALKO-11-4R, Meth-134 and Meth-135, in which calcium aluminate plays the role of the adhesive, have a minimum level of internal microstresses, which contributes to the high mechanical strength after the catalyst's activation and during its operation. Note that the service life of a catalyst is primarily determined by its catalytic activity and mechanical strength.

The experience of running industrial catalytic plants used in various chemical, petrochemical, metallurgical and other industries, as well as available literature data and our long-term monitoring of the industrial catalytic set-ups developed by «NIAP-Katalizator» allowed us to assess the reasons for their deactivation. The deactivation of the methanation catalysts may occur due to:

1. Irreversible poisoning associated with the interaction of the active component with the common catalyst poisons (sulfur compounds, chlorides etc.) present in the reaction medium.

2. Consequences of the thermal treatment, such as recrystallization, caking, the chemical interactions of active component with the support (e. g. resulting in the formation of the nickel-aluminum spinel $NiAl_2O_4$).

3. Loss of the active component due to the formation of volatile compounds such as tetracarbonylnickel.

4. Carbon deposition on the catalyst's surface.

5. Catalyst's surface contamination by various impurities.

The structural changes of the industrial porous catalysts are accelerated if the phase transformations occur upon the exposure to the reaction medium.

Under the working conditions of the large-capacity catalytic unit, the absorbents used to remove CO_2 from syngas or their decomposition products could possibly poison the catalyst. In industrial conditions this process occurs in the absorbers with absorbents such as aqueous alkaline solutions («Banfield» and «Karsol»), and organic absorbents such as aqueous solutions of activated monoethanolamine (MEA) or methyldiethanolamine (MDEA) [10, 11]. During the operation, carbon dioxide absorbents could get into the methanation reactor. As a result, a gradual decrease of catalytic activity may occur [12, 13].

To determine the causes of this phenomenon, we conducted studies in which the methanation catalysts were influenced by the organic absorbent MDEA.

Experimental

Industrial catalysts NIAP-07-01 (NKM-1) and the NIAP-07-07 (NKM-7), the latter being recommended for industrial use, were chosen as the objects of this research. NIAP-07-07 (NKM-7) was obtained in two states: 1 – non-calcined; 2 – calcined at 400 °C. It can be manufactured as cylindrical tablets, extrudates or in toroidal form from the same non-calcined catalyst mixture. The catalyst in the form of rings has a low gas flow resistance, which leads to significant savings of natural gas in the operation of the ammonia-synthesis units. In addition, imported catalysts Meth-135 (C13-03-3) and Meth-134 (C13-04-4) were investigated.

X-ray diffraction (XRD) studies of the phase composition and size of crystallites were performed using DRON-3 diffractometer (CuKα-radiation with graphite monochromator on reflected beam). For the phase analysis ICDD PDF-2 (1999) database was used. Thermogravimetric analysis (TGA) was performed using the optical derivatograph OD-103 with the heating rate of 5 °C/min. Total specific surface area was determined by the low-temperature nitrogen sorption in the vacuum adsorption setup. Total porosity was calculated from the data of real and theoretical density. Mechanical strength was determined on the «МП-2С» setup by crashing the granules with the uniaxial compressive force. The chemical composition and catalytic activity during the methanation were determined in the original setup at a pressure of 3 MPa by means of the techniques described in the TU2178-003-00209510. According to this internal standard, we adopt the following definition of a catalytic activity: it's a minimum temperature in °C, at which the volume fraction of CO at the output of the catalytic reactor is less than $1 \cdot 10^{-3}$ % at a pressure of 3 MPa. The other important experiment conditions are as follows: feed gas with 0.6–0.7 vol. % of CO, space velocity of the feed gas should be equal to 4000 h^{-1}, and the catalyst in the catalytic reactor should be pre-heated for 10 h at 550 °C.

The treatment of all investigated catalysts by 50 % aqueous solution of MDEA absorbent in the flow of nitrogen-hydrogen mixture (75 vol. % H_2, 25 vol. % N_2) was carried out in the original setup, schematic of which is shown in Fig. 1.

Before the experiments catalysts were activated in a stream of nitrogen-hydrogen mixture (NHM) at 400 °C for 5 h. At

the end of the activation process the samples were exposed to aqueous solution of MDEA in the stream of NHM in the layer catalyst at a temperature of 320 °C.

Results and discussion

In order to determine the influence of the absorbents on the catalysts' properties their initial characteristics were determined (Table 1). Data given in Table 1 show that the catalysts under investigation possess 27–40 wt. % of the Ni-containing active component with weight percentage calculated implying that NiO is the active component's only form. The average NiO particle size in NIAP-07-01 (NKM-1) and NIAP-07-07 (NKM-7) is around 60–80 Å. Total porosity is almost equal for all catalysts, its value being around 48–57 %. The only exception is NIAP-07-07, for which it's 29 %. Note that the porous structure of this catalyst forms during the combined calcination and activation process, which could explain this unique porosity value. All catalysts have quite large total surface area, with the largest value of 180 m^2/g corresponding to NIAP-07-01 (NKM-1).

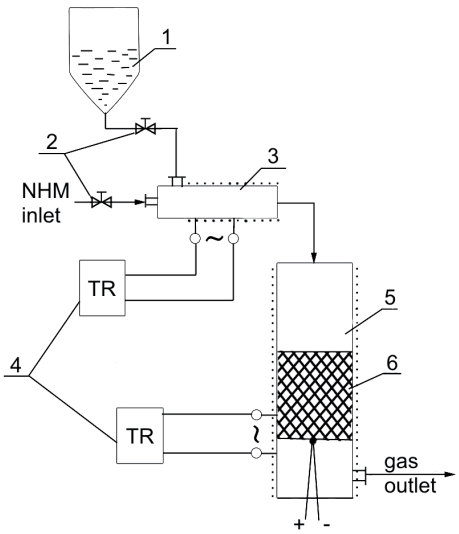

Fig. 1. Schematic diagram of a setup for catalyst treatment by the aqueous solution of the absorbent in the flow of nitrogen-hydrogen mixture (NHM):
1 – MDEA solution; 2 – flow regulators; 3 – evaporator; 4 – temperature regulators; 5 – reactor; 6 – catalyst

It should be noted that the mechanical strength of studied samples, which is one of the parameters determining the service life of a catalyst, varies significantly. The «strongest» catalyst is NIAP-07-07 (NKM-7) – 60 MPa, followed by NIAP-07-01 (NKM-1) – 29 MPa. Strength of the Meth-134 and Meth-135 is almost equal.

Phase composition and NiO particle size analysis (Table 1) shows that the aluminate cement is one of the components of the support for Meth-134, Meth-135 and NIAP-07-07 (NKM-7) catalysts. As the second component of the support for NIAP-07 (NKM) is γ-Al_2O_3, for the Meth-134 and Meth-135 catalysts it consists of the mixture of boehmite (AlOOH) and γ-Al_2O_3. Boehmite as a support constituent could impede the catalyst's activity as it inhibits the interaction between support and the active component.

The active component of raw NIAP-07-07 catalyst is a complex compound – nickel hydroxocarboaluminate (NHCA). It's the main difference between the raw NIAP-07-07 and NIAP-07-01, fired NIAP-07-07 and Meth catalysts. Activation of NIAP-07-07, coupled with the NHCA decomposition, occurs at the lower temperatures (thus – at milder conditions) as compared to the other industrial catalysts with NiO as an active component.

Since the industrial catalytic reactors are operated at about 280–320 °C, we had to determine the thermal stability of

Table 1

Physico-mechanical and physico-chemical characteristics of the original catalysts for the methanation: P – porosity, S – specific surface area

Brand of the catalyst	The geometric dimensions, mm	Bulk density, kg/dm^3	Mechanical strength, MPa P_{avg}/P_{min}	S, m^2/g	P, %	XRD phase analysis results	L_{NiO}, Å	Chem. composition, % mass.		
								NiO	Al_2O_3	CaO
NIAP-07-01 (NKM-1)	Tablet 6×5	1.08	29/20	180	57	γ-Al_2O_3, NiO, graphite	60	33.6	61.3	–
NIAP-07-07 (NKM-7)	Tablet 6×5	1.2	60/52	102	29	NHCA, graphite, $CaCO_3$ (aragonite) – not much, $Al(OH)_3$, $CaO{\cdot}2Al_2O_3$ – not much	–	30.3	25.2	7.9
NIAP-07-07 (NKM-7) fired at 450 °C	Tablet 6×5	1.1	49/32	160	53	NiO, γ-Al_2O_3, $CaO{\cdot}Al_2O_3$, $CaO{\cdot}2Al_2O_3$, graphite	75	30.3		
Meth-134 (C13-04-4)	Sphere d = 4.3	0.95	8/4	150	48	NiO, AlOOH, γ-Al_2O_3, $CaCO_3$ (boehmite)	80	27.2	57.3	10.0
Meth-135 (C13-03-3)	Sphere d = 5.3	0.99	6/1	120	54	NiO, AlOOH, γ-Al_2O_3, $CaCO_3$ (boehmite)	80	40.4	42.9	11.2

MDEA in this temperature range. Therefore, the sample of α-Al_2O_3 impregnated with the aqueous solution of MDEA was investigated by means of thermogravimetric analysis. On the differential thermogravimetric (DTG) curve, shown in Fig. 2, two distinct minima at the temperatures of 100 °C and 210 °C can be observed. They correspond to the maximum speed of removal of water from the sample and the decomposition of MDEA, accordingly. The process of decomposition of MDEA in air, accompanied by the mass loss, starts at about 150 °C and ends at 300 °C.

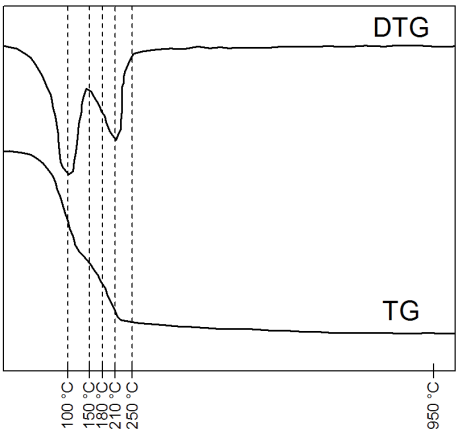

Fig. 2. TGA curve of the sample of α-alumina, impregnated with water solution of MDEA

In order to determine the optimal activation temperature of a catalyst a temperature-programmed reduction experiments were employed. It was determined that the activation is a multistage process. It should be noted that NIAP-07-07 (NKM-7) catalyst is activated at about 100 °C lower temperatures than the other studied catalysts. XRD analysis shows that at 400 °C the activation process is virtually complete. Comparison of the Ni-containing particle sizes shows that for all catalysts after the activation it still is in the range of 60–80 Å.

Physico-chemical and mechanical properties of the activated catalysts treated with MDEA solution are listed in the Table 2 along with their catalytic activities

towards the methanation. Characteristic feature of the interaction between MDEA solution and the catalyst is the initial rise of the temperature at the beginning of the reaction. It could be related to the passivation of a catalyst by the water vapor, which is formed during the evaporation of MDEA aqueous solution. XRD pattern analysis confirmed that in this case passivation of the active component occurs, effectively removing part of it from the catalysis process. The activated catalysts treated with MDEA solution in NHM gas flow contain the mixture of Ni and NiO phases, which is an evidence in favor of our assumption. Particular ratio of the mentioned phases should depend on how reduced the catalyst was and how much of metallic Ni it contains. Hence the samples before the catalytic activity measurements have been pre-treated at 400 °C for 8 h.

According to XRD, MDEA does not chemically alter the supports of the investigated catalysts for methanation. However, due to the fact that MDEA (tertiary amine) is an adsorbtion-active agent, it could negatively affect the properties of catalysts, namely, mechanical strength, specific surface area, porosity and catalytic activity. The results of our studies given in Table 2 show that after exposure to the aqueous solution of MDEA in the nitrogen-hydrogen gas mixture flow the mechanical strength and specific surface area were only insignificantly reduced. The one exception is NIAP-07-07 (NKM-7), for which the microstructure forms during the activation process. Total porosity is almost equal for all samples. Phase changes occurred during the reaction with MDEA are related to the catalysts' passivation. Comparison of the catalytic activity data show that the catalysts treated with aqueous MDEA solution in NHM flow at 320 °C retain their catalytic properties almost completely. The particular catalytic activities are comparable to those defined in our TU2178-003-00209510-2006 internal standard (typically being in the range from 170 °C to 200 °C) for methanation catalysts containing 31–40 % of active component (NiO).

Table 2

Physico-chemical and mechanical characteristics of the catalysts for methanation after exposure to MDEA

Brand of catalyst	Mechanical strength, MPa R_{SR}/P_{min}	S, m^2/g	P, %	Phase composition	Catalytic activity, °C	
					Initial samples	After exposure to MDEA
NIAP-07-01 NKM-1	27/19	155	54	NiO, Ni, graphite, γ-Al_2O_3	160	165
NIAP-07-07 NKM-7	41/35	168	41	NiO, Ni, γ-Al_2O_3, $CaO{\cdot}2Al_2O_3$, $CaCO_3$	165	170
Meth 134 (C13-04-4)	5/3	120	50	NiO, Ni, γ-Al_2O_3, $CaCO_3$	180	180
Meth 135 (C13-03-3)	5/2	66	57	Ni, NiO, γ-Al_2O_3, $CaCO_3$	175	180

Summary

In the present study raw Ni-alumina catalyst NIAP-07-01 (NKM-1) and Ni-cement-containing catalysts NIAP-07-07 (NKM-7), Meth-134 (C13-04-4) and Meth-135 (C13-03-3), as well as the same catalysts activated and pre-treated with aqueous MDEA solution in the flow of nitrogen-hydrogen gas mixture (NHM), were investigated. After the exposure to MDEA investigated catalysts almost completely retain their values of mechanical strength, specific surface area, porosity and catalytic activity, the latter being around 165–180 °C. The active component (Ni) in the catalysts subjected to the MDEA solution exposure is highly dispersed after the subsequent activation, which contributes to the elevated catalytic activity. During the treatment of a catalyst by the MDEA aqueous solution in the flow of NHM at 320 °C its passivation takes place. By using the temperature-programmed reduction it was proven that the surface of catalysts is blocked by MDEA. During the reduction of the catalysts treated with MDEA CO_2 – one of the MDEA decomposition products – is released to the gas phase, which further reinforces our assumptions.

Regeneration of the activated methanation catalysts subjected to (and inhibited by) MDEA should be carried out by drying them in the NHM at temperatures higher than 150–200 °C, followed by additional reduction at temperatures of 350–400 °C.

In Russian

Введение

В течение длительного времени в СССР, РФ и СНГ основными катализаторами, применяющимися в процессе гидрирования оксидов углерода (метанирования), являются разработанные в «НИАП-КАТАЛИЗАТОР» никель-алюминиевый катализатор марки НИАП-07-01 (НКМ-1), никель-цементсодержащий – НИАП-07-02, НИАП-07-03 (НКМ-4А) и никель-алюмохромовый ТО-2М [1–5]. Катализаторы изготавливаются по ТУ 2178-003-00209510-2006 катализаторным производством «НИАП-КАТАЛИЗАТОР», а до недавнего времени выпускались также Дорогобужской катализаторной фабрикой и Северо-Донецким катализаторным производством. В настоящее время в РФ катализаторы изготавливаются только катализаторным производством «НИАП-КАТАЛИЗАТОР». Катализаторы, произведенные в «НИАП-КАТАЛИЗАТОР», при соблюдении регламентных режимов эксплуатации работают по 15–16 лет, а на трех ПО «АЗОТ» (Невинномысск, Тольятти, Гродно) срок их службы составил 22–24 года [6].

Кроме того, применяются импортные катализаторы, основными поставщиками которых являются такие фирмы, как Haldor Topsoe, Johnson Matthey и CLARIANT (Sud-Chemie). Отечественные катализаторы изготавливаются в форме таблеток или колец (таблетирование) в соответствии с техническими требованиями ТУ 2178-003-00209510-2006 (катализаторы метанирования). Для российского рынка импортные катализаторы предлагаются в виде таблеток, а также в форме экструдатов и шариков.

Катализаторы метанирования должны иметь высокую активность в процессе гидрирования 0,3–0,7 % CO и 0,02–0,1 % CO_2 до остаточного содержания CO 5–10 ppm, термостабильность без снижения активности при перегревах до 550–650 °C, которые могут возникать в случае повышения содержания оксидов углерода в исходном газе ≥ 1 %, высокую механическую прочность и пониженное гидравлическое сопротивление.

Качество катализаторов метанирования в значительной степени определяется носителем, используемым в процессе его приготовления. В отечественных и импортных промышленных катализаторах метанирования в качестве носителя, как правило, применяют γ-Al_2O_3, алюминаты кальция, композиции CaO- MgO, γ-Al_2O_3-Cr_2O_3, γ-Al_2O_3-алюминат кальция, бемит (AlOOH) – γ-Al_2O_3 [7–9].

Содержание активного компонента (NiO) в промышленных катализаторах метанирования варьируется в пределах 25,0–45,0 масс.%. Катализаторы НИАП-07-02, НИАП-07-03, а также KATALKO-11-4R, Meth-134 и Meth-135, в которых алюминат кальция выполняет роль гидравлического вяжущего, имеют минимальный уровень внутренних микронапряжений, что способствует сохранению на высоком уровне механической прочности после стадии активации и последующего периода эксплуатации.

Срок эксплуатации катализаторов определяется в первую очередь такими показателями, как каталитическая активность и механическая прочность.

Мировой опыт эксплуатации промышленных катализаторов, применяющихся в различных процессах химической, нефтехимической, металлургической и др. отраслях, а также имеющиеся в литературе данные и наши многолетние наблюдения за работой в промышленных условиях катализаторов, разработанных в «НИАП-КАТАЛИЗАТОР», позволили во многом оценить причины их дезактивации. Дезактивация катализаторов метанирования может происходить, например, вследствие:

1. Необратимого отравления, связанного с взаимодействием активного компонента с каталитическими ядами (сернистые соединения, хлориды и т. д.), присутствующих в реакционной среде.

2. Термического воздействия – рекристаллизация, спекание, взаимодействие активного компонента с носителем. Например, образование никель-алюминиевой шпинели ($NiAl_2O_4$).

3. Унос активного компонента за счет образования летучих соединений (например, образование карбонила никеля).

4. Зауглероживание.

5. Загрязнение поверхности механическими примесями.

Структурные изменения промышленных катализаторов, которые представляют собой пористые высокодисперсные тела, ускоряются, если в них происходят фазовые превращения при воздействии реакционной среды.

В условиях работы агрегатов большой единичной мощности по производству синтетического аммиака источником катализаторных ядов могут служить абсорбенты, применяющиеся для удаления CO_2 из синтез-газа или продукты их разложения. В промышленных условиях этот процесс происходит в абсорберах с помощью таких абсорбентов, как вод-

ные щелочные растворы («Бенфийлд» и «Карсол»), а также органических поглотителей в виде водных растворов активированных моноэтаноламина (МЭА) или метилдиэтаноламина (МДЭА) [10, 11]. В процессе эксплуатации наблюдаются уносы абсорбентов диоксида углерода в реактор метанирования. Результатом этого нарушения технологического процесса, как правило, является увеличение газодинамического сопротивления метанатора и постепенное падение каталитической активности [12, 13].

Для выяснения причин этого явления нами были проведены исследования, в которых катализаторы метанирования были подвергнуты максимально жесткому воздействию органического абсорбента МДЭА.

Экспериментальная часть

В качестве объектов исследований были взяты промышленный катализатор НИАП-07-01 (НКМ-1) и рекомендуемый для промышленного внедрения катализатор НИАП-07-07 (НКМ-7) в двух его состояниях: 1 – непрокаленный; 2 – прокаленный при 400 °С. Из одной и той же непрокаленной катализаторной шихты он может изготавливаться в виде цилиндрических таблеток, экструдатов или в кольцевидной форме. Катализатор в форме колец обладает низким газодинамическим сопротивлением, что приводит к существенной экономии природного газа при эксплуатации агрегата синтеза аммиака. Кроме того, были исследованы импортные катализаторы марки Meth-135 (C13-03-3) и Meth-134 (C13-04-4).

Рентгенографические исследования с определением фазового состава и дисперсности кристаллитов проводили с использованием дифрактометра ДРОН-3 (CuKα-излучение с графитовым монохроматором на отраженном пучке). Для идентификации фаз использовали базу данных Международного комитета порошковых дифракционных стандартов (ICDD PDF-2, 1999 г.). Комплексные термические исследования осуществляли с применением оптического дериватографа марки OD-103 (линейная скорость нагрева 5 °С/мин). Общую удельную поверхность определяли по низкотемпературной адсорбции азота на вакуумной адсорбционной установке. Общую пористость рассчитывали по данным истинной и кажущейся плотности. Механическая прочность определялась на приборе «МП-2С» раздавливанием гранул с приложением нагрузки на торец. Химический состав и каталитическую активность в процессе метанирования на пилотной установке при давлении 3 МПа определяли по методикам, приведенным в ТУ 2178-003-00209510.

Химический состав и каталитическую активность в процессе метанирования на пилотной установке при давлении 3 МПа определяли по методикам, приведенным в ТУ 2178-003-00209510. За меру каталитической активности принята минимальная температура (°С), обеспечивающая объемную долю CO на выходе не более $1 \cdot 10^{-3}$ об.% при давлении 3 МПа, объемной скорости 4000 $ч^{-1}$, объемной доле в исходном газе 0,6–0,7 об.% CO после предварительного перегрева катализатора при температуре 550 °С в течение 10 ч.

Обработку всех исследуемых катализаторов 50 %-м водным раствором абсорбента МДЭА в потоке азото-водородной смеси (75 об.% H_2, 25 об.% N_2) проводили на установке, принципиальная схема которой приведена на рис. 1.

Перед проведением экспериментов осуществляли активацию катализаторов в потоке азото-водородной смеси (АВС) при температуре 400 °С в течение 5 ч. По окончании процесса активации образцы подвергали при температуре 320 °С воздействию водного раствора МДЭА в потоке АВС в слое катализатора.

Результаты и обсуждение

Для определения степени воздействия абсорбентов на катализаторы были определены их основные исходные характеристики (табл. 1).

Из данных, приведенных в табл. 1, видно, что исследуемые катализаторы имеют концентрацию активного компонента в пересчете на NiO в пределах 27–40 масс.%. Дисперсность NiO в катализаторах НИАП-07-01 (НКМ-1) и НИАП-07-07 (НКМ-7) находится на уровне 60–80 Å. Показатель общей пористости практически одинаков для всех катализаторов и находится на уровне 48–57 %. Исключение составляет катализатор НИАП-07-07, для которого значение общей пористости составляет 29 %. Это явление объясняется тем, что формирование пористой структуры этого катализатора происходит в совмещенном процессе прокаливания и активации. Сопоставление данных по общей удельной поверхности показывает, что все катализаторы имеют высокоразвитую общую удельную поверхность. Максимальное ее значение равное 180 $м^2/г$ имеет катализатор НИАП-07-01 (НКМ-1).

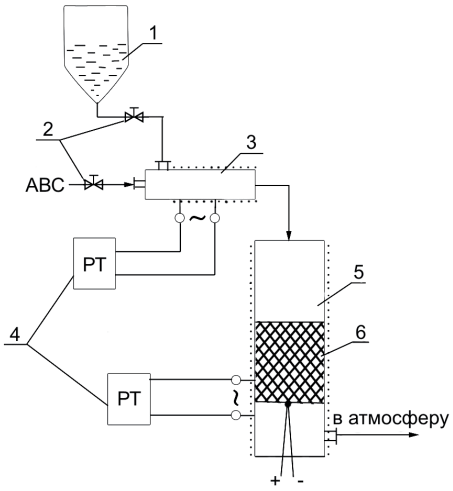

Рис. 1. Принципиальная схема установки для обработки катализатора в потоке азота или азото-водородной смеси с водными растворами абсорбентов: 1 – раствор МДЭА; 2 – регуляторы расхода; 3 – испаритель; 4 – регулятор температуры; 5 – реактор; 6 – катализатор

Можно отметить значительный разброс для катализаторов по такому показателю, как механическая прочность, которая во многом определяет срок службы катализаторов. По этому показателю наибольшее предпочтение можно отдать катализатору НИАП-07-07 (НКМ-7), для которого ее значение равно 60 МПа. На второе место можно поставить катализатор НИАП-07-01 (НКМ-1) – 29 МПа. Катализаторы Meth-134 и Meth-135 по своим прочностным показателям практически одинаковы.

Анализ фазового состава и дисперсности NiO (табл. 1) свидетельствует о том, что в качестве одного из компонентов носителя катализаторов Meth-134, Meth-135 и НИАП-07-07

(НКМ-7) применяется алюминатный цемент. Если в катализаторах серии НИАП-07 (НКМ) вторым компонентом носителя является γ-Al_2O_3, то в катализаторах Meth-134 и Meth-135 применяется смесь гидрооксида алюминия в виде его модификации «бемит» (AlOOH) и γ-Al_2O_3. Применение в катализаторах Meth-134 и Meth-135 гидрооксида алюминия в виде его модификации «бемит» приводит к недостаточно глубокому его взаимодействию с прекурсором активного компонента, что неизбежно будет сказываться на каталитической активности.

Отличие исходного образца катализатора НИАП-07-07 от НИАП-07-01 (НКМ-1), прокаленного НИАП-07-07 (НКМ-7) и катализатора марки Meth состоит в том, что его активный компонент находится в виде сложного химического соединения (гидроксокарбоалюминат никеля – ГКАН). Активация этого катализатора, совмещенная с разложением ГКАН, происходит при более низких температурах и в более мягких условиях по сравнению с другими промышленными катализаторами, в которых активный компонент находится в оксидной форме.

Так как эксплуатация катализаторов в промышленных условиях агрегатов синтеза аммиака осуществляется при температурах 280–320 °С, в этом же температурном интервале была определена термическая устойчивость МДЭА, данные по которой в справочной литературе отсутствуют. С этой целью образец α-Al_2O_3 был пропитан до состояния насыщения водным раствором МДЭА, который затем был исследован дериватографическим методом анализа. На рис. 2 приведена дериватограмма данного образца.

Таблица 1

Физико-механические и физико-химические характеристики исходных катализаторов метанирования: П – пористость, Syд – удельная поверхность, LNiO – дисперсность частиц NiO

Марка катализатора	Геометрические размеры, мм	Насыпная плотность, кг/дм^3	Механическая прочность, МПа на торец $P_{ср.}/P_{min}$	Syд., м^2/г	П, %	РФА	L_{NiO}, Å	Хим. состав, % масс.		
									Al_2O_3	CaO
НИАП-07-01 (НКМ-1)	Таблетка 6×5	1,08	29/20	180	57	γ-Al_2O_3, NiO, графит	60	33,6	61,3	–
НИАП-07-07 (НКМ-7)	Таблетка 6×5	1,2	60/52	102	29	ГКАН, графит, $CaCO_3$ (арагонит) – мало, $Al(OH)_3$, $CaO{\cdot}2Al_2O_3$ – мало	–	30,3	25,2	7.9
НИАП-07-07 (НКМ-7) прокален при 450 °С	Таблетка 6×5	1,1	49/32	160	53	NiO, γ-Al_2O_3, $CaO{\cdot}Al_2O_3$, $CaO{\cdot}2Al_2O_3$, графит	75	30,3	–	–
Meth-134 (C13-04-4)	Шарик d = 4,3	0,95	8/4	150	48	NiO, AlOOH, γ-Al_2O_3, $CaCO_3$ (бемит)	80	27,2	57,3	10,0
Meth-135 (C13-03-3)	Шарик d = 5,3	0,99	6/1	120	54	NiO, AlOOH, γ-Al_2O_3, $CaCO_3$ (бемит)	80	40,4	42,9	11,2

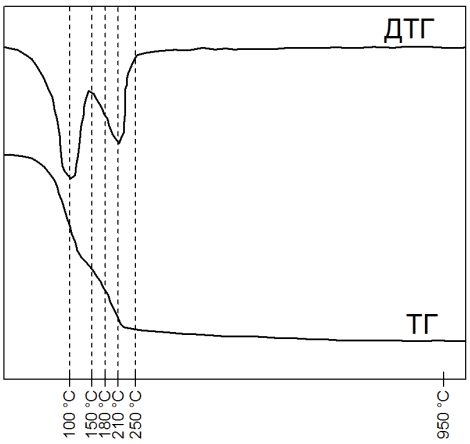

Рис. 2. Дериватограмма образца α-Al_2O_3, пропитанного до состояния насыщения раствором МДЭА

На дериватограмме имеются два ярко выраженных эффекта с характеристическими температурами T_{max} = 100 °C и T_{max} = 210 °C, которые соответствуют удалению из образца физически связанной влаги и разложению МДЭА. Процесс разложения МДЭА в среде воздуха сопровождается убылью массы. Начинается он при температуре 150 °C, а его максимальная скорость достигается при 210 °C. Заканчивается разложение МДЭА при 300 °C.

Для определения оптимальной температуры активации катализаторов были проведены исследования температурно-программированного восстановления. Было установлено, что этот процесс является многостадийным. Кроме того, было обнаружено, что катализатор НИАП-07-07 (НКМ-7) активируется ~ на 100 °C ниже всех исследованных образцов. Рентгенографические данные показали, что при температуре 400 °C происходит практически полная активация. Сопоставление данных по дисперсности Ni свидетельствует о том, что она для всех исследуемых катализаторов практически одинакова и находится в пределах 60÷80 Å.

В табл. 2 приведены физико-механические и физико-химические характеристики активированных исследуемых катализаторов метанирования с последующим воздействием на них водного раствора МДЭА в потоке АВС, а также их каталитическая активность в процессе метанирования. Характерной особенностью экспериментов по воздействию водного раствора МДЭА на активированные катализаторы метанирования было то, что в начальный

Таблица 2

Физико-механические и физико-химические характеристики катализаторов метанирования после обработки МДЭА

Марка катализатора	Механическая прочность, МПа на торец $P_{ср.}/P_{min}$	Sуд., м²/г	П, %	РФА	Активность, $T_{пр.}$, °C	
					Исходных образцов	После воздействия МДЭА
НИАП-07-01 НКМ-1	27/19	155	54	NiO, Ni, графит, γ-Al_2O_3	160	165
НИАП-07-07 НКМ-7	41/35	168	41	NiO, Ni, γ-Al_2O_3, $CaO{\cdot}2Al_2O_3$, $CaCO_3$	165	170
Meth-134 (C13-04-4)	5/3	120	50	NiO, Ni, γ-Al_2O_3, $CaCO_3$	180	180
Meth-135 (C13-03-3)	5/2	66	57	Ni, NiO, γ-Al_2O_3, $CaCO_3$	175	180

период подачи МДЭА в потоке АВС наблюдался рост температуры в слое катализатора, что связано с пассивирующим действием водяного пара, образующегося при испарении водного раствора МДЭА. Анализ дифрактограмм подтвердил что, в данном случае происходит пассивация активного компонента Ni и определенная его часть выводится из каталитического процесса. Свидетельством этого является наличие в фазовом составе активированных катализаторов, подвергнутых воздействию водного раствора МДЭА в потоке АВС, фаз Ni и NiO. Соотношение этих фаз, по всей видимости, зависит от степени восстановленности и от содержания металлического никеля в каждом конкретном катализаторе. Исходя из этого, образцы перед проведением испытаний активности были предварительно восстановлены при 400 °С в течение 8 ч.

По данным РФА, МДЭА не оказывает химического воздействия на носители исследуемых катализаторов метанирования. Однако в связи с тем, что МДЭА (третичный амин) является адсорбционно-активным веществом, он может негативно сказаться на свойствах катализаторов, и в первую очередь на таких его характеристиках, как механическая прочность, общая удельная поверхность, пористость и каталитическая активность. Результаты исследований, приведенные в табл. 2, показывают, что после воздействия на активированные катализаторы водного раствора МДЭА с одновременным потоком АВС произошло незначительное снижение механической прочности и общей удельной поверхности. Исключение составляет катализатор НИАП-07-07 (НКМ-7), у которого формирование текстуры происходит в процессе активации. Общая пористость для всех образцов практически одинакова. Произошли изменения в фазовом составе, связанные с процессом пассивации катализаторов. Сравнение данных по каталитической активности, полученных в данном эксперименте, показывает, что катализаторы, подвергнутые при 320 °С воздействию водного раствора МДЭА в потоке АВС после предварительной активации, практически не теряют своих каталитических свойств. Данный показатель хорошо сопоставим со значениями активности (по ТУ 2178-003-00209510-2006) катализаторов метанирования, имеющих содержание активного компонента (NiO) от 31 до 40 %. Для катализаторов с таким содержанием активного компонента каталитическая активность находится в пределах от 170 до 200 °С.

Выводы

Комплексом физико-механических и физико-химических методов исследованы характеристики Ni-Al катализатора НИАП-07-01 (НКМ-1) и Ni-цементсодержащих катализаторов марки НИАП-07-07 (НКМ-7), Meth-134 (С13-04-4) и Meth-135 (С13-03-3) как исходных катализаторов, так и активированных с последующим воздействием на них водного раствора МДЭА в потоке АВС. Исследуемые катализаторы после воздействия на них водного раствора МДЭА в потоке АВС практически сохраняют высокие значения механической прочности, общей удельной поверхности, пористости

и каталитической активности, которая находится на уровне 165–180 °С. Установлено, что активный компонент (Ni) в катализаторах, обработанных МДЭА с последующей активацией, находится в дисперсном состоянии, что предопределяет их высокую каталитическую активность. В процессе воздействия на активированные катализаторы при температуре 320 °С водного раствора МДЭА в потоке АВС происходит их пассивация. Методом температурно-программированного восстановления установлено, что поверхность катализаторов блокируется МДЭА. Это предположение подтверждается выделением в процессе восстановления обработанных катализаторов в газовую фазу CO_2, являющегося одним из продуктов разложения МДЭА.

Регенерация в промышленных условиях активированных катализаторов метанирования, подвергшихся воздействию водного раствора МДЭА, должна осуществляться путем их сушки в потоке АВС при температурах не ниже 150–200 °С с последующим довосстановлением при температурах 350–400 °С.

References

1. Golosman EZ, Efremov VN, Kreyndel' AI, Mironov YuV, Obysov AV, Sobolevskiy VS, Yakerson VI, inventors; Men'shov VN, assignee. Russian Federation patent RU2143320. 27.12.1999. Russian.
2. Golosman EZ, Efremov VN. Promyshlennye katalizatory gidrirovaniya oksidov ugleroda [Industrial catalysts for the carbon oxides hydrogenation]. *Kataliz v promyshlennosti*. 2012;(5):36-55. Russian. DOI:10.18412/1816–0387-2012-5-36-55.
3. Alekseev AM. Iz istorii kataliza [History of catalysis]. Moscow: Kal'vis, 2005. [Chapter], GIAP v istorii katalizatornoy promyshlennosti SSSR i Rossii [GIAP in the history of catalysis industry of USSR and Russia]; p. 481–532. Russian.
4. Melnikov EYa, editor. Spravochnik azotchika. 2nd ed. Moscow: Chemistry, 1987. 512 p. Russian.
5. Demidenko IM, Yankovskiy NA, Stepanov VA, Nikitina EF, Kravchenko BV. Katalizatory i protsessy s ikh primeneniem v azotnoy promyshlennosti [Catalysts and processes with their application in the nitric industry]. Gorlovka: Gorlovskaya tipografiya, 1998. 198 p. Russian.
6. Efremov VN, Kashinskaya AV, Polivanov BI, Boevskaya EA, Golosman EZ. O razrushenii katalizatora metanirovaniya pod vozdeystviem vodnogo rastvora potasha [Destruction of the methanation catalyst by water solution of KOH. Part I: The nickel-alumina catalyst NIAP-07-01 (NKM-1)]. *Neftegazokhimiya*. 2015;4:62–6. Russian.
7. Takenara S, Shimizu T, Otsuka K. Complete removal of carbon monoxide in hydrogen-rich gas stream through methanation over supported metal catalysts. *Int J Hydrogen Energy.* 2004;29(10):1065–73. DOI:10.1016/j.ijhydene.2003.10.009.
8. Men Y, Kolb G, Zapf R, Hessel V, Love H. Selective methanation of carbon oxides in a microchannel reactor-Primary screening and impact of gas additives. *Catal Today.* 2007;125(1-2):81–7. DOI:10.1016/j.cattod.2007.02.017.

9. Liu Q, Dong X, Mo X, Lin W. Selective catalyc methanation of CO in hydrogen-rich gases over Ni/ZrO_2 catalyst. *J Natur Gas Chem*. 2008;17(3):268–72. DOI:10.1016/S1003-9953(08)60062-6.
10. Leites IL, Avetisov AK, Yazvikova NV, Suvorkin SV, Baichtok CK, Dudakova NV, Deev KN, Kosarev GV. Issledovanie fiziko-khimicheskikh svoystv modifitsirovannogo MEDA-absorbenta dlya tonkoy ochistki gaza ot dioksida ugleroda v proizvodstve ammiaka [Investigation of physico-chemical properies of modified MDEA-absorbent for fine purification of gas from carbon dioxide in ammonia production]. *Khimicheskaya promyshlennost' segodnya*. 2003;1:34–41. Russian.
11. Avetisov AK, Kononov SM, Sokolov AM, Baichtok CK, Suvorkin SV, Leites IL, Deripasov VV, Sokolinskiy CA, Yazvikova NV. Opyt modernizatsii otdeleniya absorbtsionnoy ochistki agregata sinteza ammiaka AM-70 na OAO «Nevinnomysskiy Azot» s zamenoy MEA-rastvora na MDEA-absorbent rossiyskogo proizvodstva [Experience of modernization of absorption purification unit of the ammonia-synthesis plant AM-70 at JSC «Nevinnomysskiy Azot»: replacement of the MEA solution by MDEA-absorbent made in Russia]. *Khimicheskaya promyshlennost' segodnya*. 2003;2:22–4. Russian.
12. Vakk EG, Shuklin GV, Leites IL. Poluchenie tekhnologicheskogo gaza dlya proizvodstva ammiaka, metanola, vodoroda i vysshikh uglevodorodov. Teoreticheskie osnovy, tekhnologiya, katalizatory, oborudovanie, sistemy upravleniya [Obtaining of gas for production of ammonia, methanol, hydrogen and higher hydrocarbons. Theoretical foundations, technology, catalysts, equipment, management: a textbook]. Moscow, 2001. 478 p. ISBN978-5-98801-033-3. Russian.
13. Efremov VN, Golosman EZ, Polivanov BI, Kashinskaya AV, Polushin AP. Ustoychivost' nikelevykh promyshlennykh katalizatorov metanirovaniya k vozdeystviyu aktivirovannogo metildietanolamina – absorbent CO_2 [Stability of Industrial Nickel Catalysts for Methanation against the Action of Activated Methyldiethanol Amine used as CO_2 Absorbent]. *Kataliz v promyshlennosti*. 2016;16(4):67–76. Russian. DOI:10.18412/1816-0387-2016-4-67-76.

Cite this article as:
Efremov VN, Golosman EZ, Kashinskaya AV, Mugenov TI, Zolotareva VE, Polivanov BI, Polushin AP. Resistance of industrial nickel-containing methanation catalysts to the poisoning by organic carbon dioxide absorbents. *Chimica Techno Acta.* 2017;4(3):167–82. DOI:10.15826/chimtech/2017.4.3.02.

Sednev A. L., Tsvetkov D. S.
Chimica Techno Acta. 2017. Vol. 4, No. 3. P. 183–190.
ISSN 2409–5613

A.L. Sednev, D.S. Tsvetkov

Institute of Natural Sciences and Mathematics,
Ural Federal University, 19 Mira St.,
Ekaterinburg, 620002, Russia
e-mail: Anton.Sednev@urfu.ru

DOI: 10.15826/chimtech/2017.4.3.03

Study and optimization of the synthesis routine of the single phase $YBaCo_2O_{6-\delta}$ double perovskite

The chemical interaction of $YCoO_{3-\delta}$ and $BaCoO_{3-\delta}$ with formation of double perovskite was studied depending on temperature and oxygen partial pressure. The stability of $YCoO_3$ was shown to have a crucial influence on the kinetics and mechanism of $YBaCo_2O_{6-\delta}$ formation. It was found that at 1000 °C in air, i.e. under conditions when $YCoO_3$ is unstable, the double perovskite $YBaCo_2O_{6-\delta}$ is formed much slower compared to the pure oxygen atmosphere where $YCoO_3$ is stable at the same temperature. Thus controlling $YCoO_3$ stability was shown to be the factor of key importance for optimal preparation of the $YBaCo_2O_{6-\delta}$ single phase.

Keywords: $YBaCo_2O_6$ synthesis, $YCoO_3$ instability, pO_2 acceleration, double perovskite synthesis, $YBaCo_2O_5$, $YCoO_3$, $BaCoO_3$.

Received: 07.09.2017; accepted: 25.09.2017; published: 20.10.2017.

Introduction

Complex oxide $YBaCo_2O_{6-\delta}$ with double perovskite structure has been extensively investigated in recent years as a promising material for oxygen membranes [1, 2] and solid oxide fuel cells (SOFCs) [3, 6, 7, 9, 12] due to high mixed ionic-electronic conductivity [12] and moderate thermal expansion comparable to that of the state-of-the art SOFC electrolytes [3]. However, $YBaCo_2O_{6-\delta}$ is unstable in air at temperatures between 800 and 850 °C [13] and decomposes to mixture of the simple perovskites $YCoO_{3-\delta}$ and $BaCoO_{3-\delta}$, which are more thermodynamically stable under these conditions. This significantly impedes obtaining a single phase material. Moreover, a synthesis routine, which could be provided the single phase $YBaCo_2O_{6-\delta}$ obtaining, has not been discussed in literature so far. The lack of the appropriate data also inhibits a commercial application of the $YBaCo_2O_{6-\delta}$ based materials.

Therefore the main aim of the current work was to study a formation of the $YBaCo_2O_{6-\delta}$ double perovskite at 900 and 1000 °C in different gas atmospheres in order to optimize its synthesis routine.

Experimental

Taking into account that synthesis of $YBaCo_2O_{6-\delta}$ proceeds through the formation of intermediate phases of $YCoO_{3-\delta}$ and $BaCoO_{3-\delta}$ like other double perovs-

kites $LnBaCo_2O_{6-\delta}$ [14] as well as that a synthesis routine for these intermediate phases has been already described in literature [15, 16] we selected $YCoO_{3-\delta}$ and $BaCoO_{3-\delta}$ as starting reagents for preparation of the $YBaCo_2O_{6-\delta}$ double perovskite.

Powder samples of $YCoO_{3-\delta}$, $BaCoO_{3-\delta}$ were synthesizes by means of glycerol-nitrate technique, using Co, Y_2O_3 and $BaCO_3$ as starting materials. All the materials used had a purity of 99.99 %. Metallic Co was obtained by reduction of Co_3O_4 (purity 99.99 %) in H_2 atmosphere at 600 °C. Y_2O_3 and $BaCO_3$ were preliminary calcined at 1100 °C and 600 °C, respectively, in air for two hours in order to remove adsorbed H_2O and CO_2. Stoichiometric mixture of starting materials was dissolved in concentrated nitric acid. Then the required quantity of glycerol as a complexing and reducing agent was added to the obtained solution. Afterwards the solution was evaporated to dryness, and resulted dry powder was pyrolyzed. The product of pyrolysis was put in a crucible and calcined in a furnace. The final calcination was carried out at 1100 °C in air for two hours C for $BaCoO_{3-\delta}$ and at 900 °C for $YCoO_{3-\delta}$. Phase composition of the as-prepared powder samples was confirmed by X-ray diffraction using Shimadzu XRD-7000 diffractometer (CuKα radiation, 20≤2θ, °≤90). X-ray diffraction patterns of the as-synthesized $YCoO_{3-\delta}$ and $BaCoO_{3-\delta}$ are shown in Figs. 1 and 2.

The results of the structureless Le Bail fitting are also shown in Fig. 1 and 2. It should be noted that the X-ray diffraction pattern of $BaCoO_3$ was interpreted as a mixture of two compounds: $BaCoO_3$ and $BaCoO_{2.61}$ (see Fig. 2). The refined cell parameters of the prepared compounds given in Table 1 are in a good agreement with those reported in literature.

Synthesis of $YBaCo_2O_{6-\delta}$ was studied by annealing equimolar mixture of $YCoO_{3-\delta}$ and $BaCoO_{3-\delta}$ for 72h (6 steps with duration of 12 h at each step) at temperatures 900 and 1000 °C in atmospheres with oxygen partial pressure (pO_2)

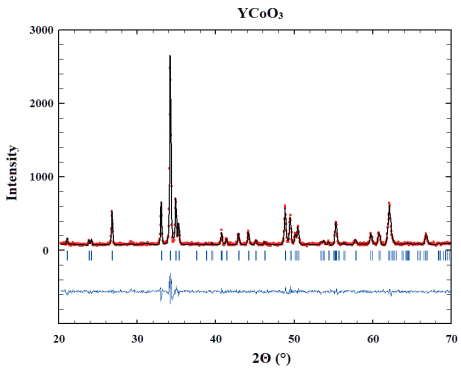

Fig. 1. X-ray diffraction pattern and its matching refinement plot of $YCoO_{3-\delta}$: observed X-ray diffraction intensity – points and calculated curve ($\chi^2 = 1.62$) – line. The bottom curve is the difference of patterns, $y_{obs} - y_{cal}$, and the small bars indicate the angular positions of the allowed Bragg reflections

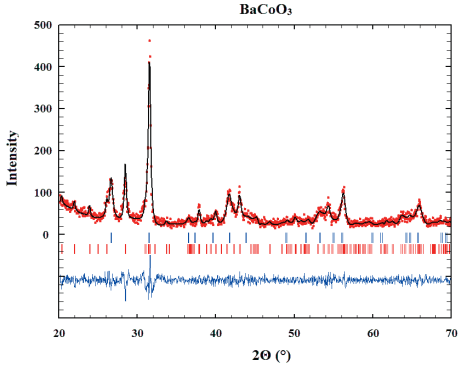

Fig. 2. X-ray diffraction pattern and its matching refinement plot of $BaCoO_{3-\delta}$: observed X-ray diffraction intensity - points and calculated curve ($\chi^2 = 1.87$) – line. The bottom curve is the difference of patterns, $y_{obs} - y_{cal}$, and the small bars indicate the angular positions of the allowed Bragg reflections for $BaCoO_3$ (blue lines) and $BaCoO_{2.61}$ (red lines)

0.21 and 1 atm with intermediate mixture regrinding in agate mortar. Phase composition of the samples after each step of annealing was controlled by XRD.

Table 1

Crystallographic parameters of synthesized cobaltites in comparison with literature data

Compound	Space group	a^*, Å	b^*, Å	c^*, Å	Reference
$YCoO_{3-\delta}$	Pbnm	5.139	5.419	7.365	this work
		5.137	5.420	7.364	[17]
		5.132	5.411	7.360	[18]
$BaCoO_3$	P-6m2	5.683	5.683	4.552	this work
		5.645	5.645	4.752	[19]
		5.652	5.6525	4.763	[20]
$BaCoO_{2.63}$	P63/mmc	5.666	5.666	28.494	this work
		5.665	5.665	28.493	[16]
		5.671	5.671	28.545	[21]

* uncertainty ±0.001 Å.

Results and discussion

Fig. 3 shows XRD patterns of the $YCoO_{3-\delta}$ + $BaCoO_{3-\delta}$ equimolar mixtures annealed at 900 °C in air (pO_2 = 0.21 atm) and pure oxygen (pO_2 = 1 atm) for 72 h. As seen annealing neither in air nor in oxygen atmosphere leads to formation of the single phase $YBaCo_2O_{6-\delta}$ at least for this time of annealing.

Moreover XRD pattern of the mixture annealed at 900 °C in pure oxygen atmosphere does not show any indication of the chemical interaction between the reagents and formation of $YBaCo_2O_{6-\delta}$ double perovskite whereas annealing in air leads to formation of significant amount of this double perovskite (see Fig. 3). Possible reason of this difference seems to be related to the instability of $YBaCo_2O_{6-\delta}$ oxide under oxidizing conditions at temperatures lower than some threshold value [11–13].

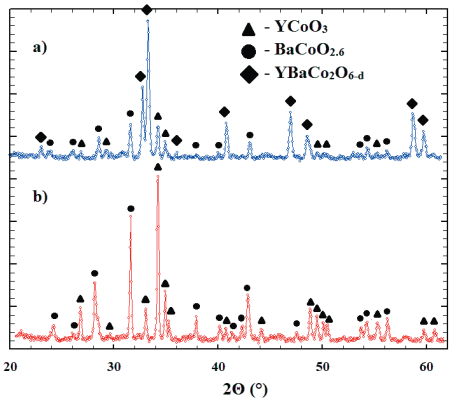

Fig. 3. XRD patterns of $YCoO_{3-\delta}$ and $BaCoO_{3-\delta}$ equimolar mixtures after annealing in air (a) and pure oxygen (b) at 900 °C for 72 h

Figs. 4 and 5 show XRD patterns of the $YCoO_{3-\delta}$ and $BaCoO_{3-\delta}$ equimolar mixtures annealed at 1000 °C in air (pO_2 = 0.21 atm) and pure oxygen (pO_2 = 1 atm) for 72 h. As seen annealing in air also did not lead to the formation of the single phase double perovskite. Y_2O_3, $BaCoO_3$ and CoO can be identified as impurities in the X-ray diffraction pattern shown in Fig. 4. The presence of these impurities is a consequence of instability of the $YCoO_3$, which decomposes in air at $T \geq 900$ °C with formation of Y_2O_3 and CoO [11–13, 22, 23]. Similar behavior is well-known for the perovskite-type cobaltites with small rare-earth elements [24, 25].

Therefore formation of $YBaCo_2O_{6-\delta}$ at 1000 °C in air seems to proceed according

to the two-stage process. First $YCoO_3$ decomposes into Y_2O_3 and CoO upon heating of the equimolar mixture of $YCoO_{3-\delta}$ and $BaCoO_{3-\delta}$ up to 1000 °C in air

$$YCoO_3 = ½Y_2O_3 + CoO + ¼O_2. \quad (1)$$

Then a mixture of Y_2O_3, $BaCoO_3$ and CoO slowly reacts at 1000 °C with formation of the required double perovskite

$$½Y_2O_3 + BaCoO_{3-\delta} + CoO = \\ = YBaCo_2O_{6-\delta} + ¼O_2. \quad (2)$$

At the same time annealing the $YCoO_{3-\delta}$ and $BaCoO_{3-\delta}$ equimolar mixture at 1000 °C in oxygen for 72 h leads to formation of the single phase $YBaCo_2O_{6-\delta}$ as seen in Fig. 5 where appropriate XRD pattern is shown. This pattern was refined as a mixture of two phases having 3×2×2 and 1×2×2 superstructures. The former has tetragonal structure (s. g. P4/mmm) with cell parameters $\boldsymbol{a} = \boldsymbol{b} = 11.596(4)$ Å and $\boldsymbol{c} = 7.509(7)$ Å whereas the latter has orthorhombic structure (s. g. Pmma) with cell parameters $\boldsymbol{a} = 3.821(4)$ Å, $\boldsymbol{b} = 7.846(2)$ Å, $\boldsymbol{c} = 7.515(8)$ Å in full agreement with available structural data [5, 7, 12, 26, 27].

Detailed step-by-step investigation of the $YBaCo_2O_{6-\delta}$ synthesis in oxygen at this temperature revealed that the resultant mixture at each step except last one contained $BaCoO_{3-\delta}$, Y_2O_3, CoO, $YCoO_{3-\delta}$ and the product $YBaCo_2O_{6-\delta}$. This result can be understood, first of all, based on the analysis of the thermodynamics of reaction Eq. (1). Although for this particular reaction thermodynamic functions are unknown similar reactions for Ho- and Er-contained cobaltites have already been studied in this respect [24, 25]. Required thermodynamic data for them are given in Table 2. As seen $HoCoO_3$ decomposition starts at 1051 °C in air whereas $ErCoO_3$ decomposes already at 866 °C in the same atmosphere. $YCoO_3$ as mentioned above is somewhere between these two compounds since its decomposition in air starts at 900–950 °C [11–13, 22, 23]. Therefore standard enthalpy and entropy of reaction Eq. (1) for $YCoO_3$ may be roughly estimated by averaging corresponding standard enthalpies and entropies for Er- and Ho-containing cobaltites.

The thermodynamic quantities of reaction Eq. (1) obtained in this way are also

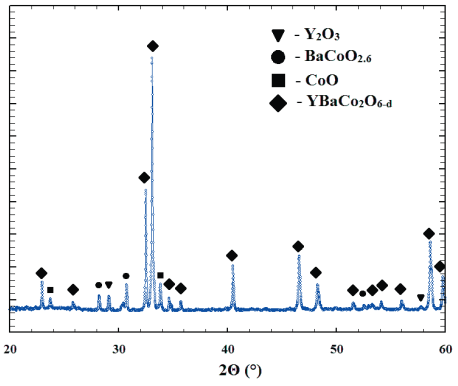

Fig. 4. XRD pattern of $YCoO_{3-\delta}$ and $BaCoO_{3-\delta}$ equimolar mixtures annealed in air at 1000 °C for 72 h

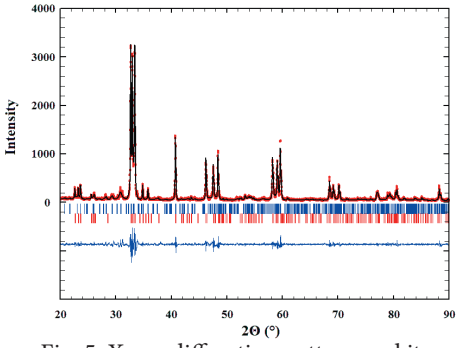

Fig. 5. X-ray diffraction pattern and its matching refinement plot of $YBaCo_2O_{6-\delta}$ obtained by annealing at 1000 °C in oxygen for 72 h: observed X-ray diffraction intensity – points and calculated curve – line. The bottom curve is the difference of patterns, $y_{obs} - y_{cal}$, and the small bars indicate the angular positions of the allowed Bragg reflections for $YBaCo_2O_{6-\delta}$ with 3×2×2 superstructure (blue) and 1×2×2 superstructure (red)

shown in Table 2. They allow estimating corresponding equilibrium decomposition temperatures for $YCoO_3$ in air and oxygen. As seen in Table 2 this estimation gives 953 °C as the decomposition temperature of $YCoO_3$ in air, which is in line with that reported earlier [11–13, 22, 23]. The value of decomposition temperature in oxygen is around of 1060 °C. Taking into account that this is only a very rough estimation one may expect the real decomposition temperature for $YCoO_3$ in oxygen in the range of 1000–1100 °C, i. e. during annealing of the $YCoO_{3-\delta}$ and $BaCoO_{3-\delta}$ equimolar mixture at 1000 °C

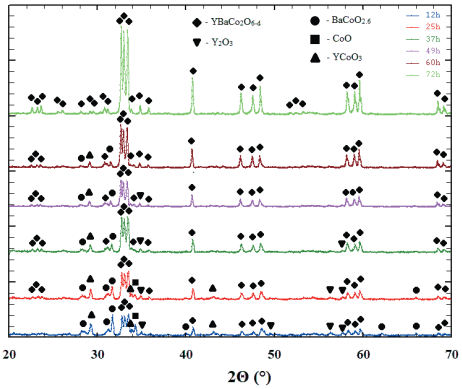

Fig. 6. XRD patterns of $YCoO_{3-\delta}$ and $BaCoO_{3-\delta}$ equimolar mixture step-by-step annealed at 1000 °C in pure oxygen

Table 2

Thermodynamics of reaction Eq. (1) for the selected cobaltites at 927 °C

	$\Delta H°$, kJ·mol^{-1}	$\Delta S°$, J·mol^{-1}·K^{-1}	T_{air}*, °C	T_{O2}**, °C	Reference
$HoCoO_3$	44.88	30.63	1051	1192	[24, 25]
$ErCoO_3$	51.34	41.3	866	970	[24, 25]
$YCoO_3$	48	36	953	1060	Estimated in this work

* Equilibrium temperature for $RCoO_3$ (R = Y, Ho, Er) decomposition in air
** Equilibrium temperature for $RCoO_3$ (R = Y, Ho, Er) decomposition in oxygen

in pure oxygen atmosphere its first component is in equilibrium with oxides Y_2O_3 and Co O. Therefore synthesis of the $YBaCo_2O_{6-\delta}$ double perovskite under these conditions can be described by the following parallel reactions

$$YCoO_3 + BaCoO_3 = YBaCo_2O_6 \quad (3)$$

$$½Y_2O_3 + CoO + ¼O_2 = YCoO_3 \quad (4)$$

The equilibrium of reaction Eq. (4) is shifted to the right due to consumption of $YCoO_3$ as a reagent of reaction Eq. (3).

Comparison of the results of synthesis at 1000 °C in two atmospheres, i. e. air and oxygen, shows that in the second case formation of the double perovskite occurs apparently faster. One may speculate on the reasons of the observed positive influence of high oxygen pressure. Intuitively it seems quite expected that the combination (or interaction) of two 'simple' perovskites representing elementary 'building' units of the double perovskite structure is a faster process then a combination of barium cobaltite with two oxides. Significant diffusion difficulties are quite expected in the last case. However the exact reasons and detailed microscopic mechanism of an interaction in oxygen or air atmosphere should be studied in order to make meaningful conclusions. We only would like to emphasize once again the key role, which thermodynamic stability of $YCoO_3$ plays in the optimization of synthesis routine for the $YBaCo_2O_{6-\delta}$ double perovskite.

Conclusions

Synthesis of $YBaCo_2O_{6-\delta}$ from equimolar mixture of $YCoO_3$ and $BaCoO_{3-\delta}$ was studied at 900 °C and 1000 °C in air and pure oxygen atmosphere. It was shown that synthesis at 1000 °C in pure oxygen atmosphere is an optimal way of obtaining the single phase $YBaCo_2O_{6-\delta}$. Detailed step-by-step investigation of the synthesis was carried out at 1000 °C in pO_2 = 1 atm. The mechanism of $YBaCo_2O_{6-\delta}$ synthesis in different gas atmospheres was proposed based on thermodynamics of $YCoO_3$ and crucial role of this oxide stability in governing of the synthesis process was revealed.

References

1. Haoshan H, Lu Z, Yingfan W, Shijiang L, Xing H. Thermogravimetric study on oxygen adsorption/desorption properties of double perovskite structure oxides $REBaCo_2O_{5+\delta}$ (RE = Pr, Gd, Y). *J Rare Earths.* 2007;25:275–81. DOI:10.1016/S1002-0721(07)60421-9.
2. Hao H, Chen B, Zhao L, Hu X. Oxygen removal from nitrogen using $YBaCo_2O_{5+\delta}$ adsorbent. *Korean J Chem Eng.* 2011;28(2):563-66. DOI:10.1007/s11814-010-0354-9.
3. Xue J, Shen Y, He T. Double-perovskites $YBaCo_{2-x}Fe_xO_{5+\delta}$ cathodes for intermediate-temperature solid oxide fuel cells. *J Power Sources.* 2011;196(8):3729-35. DOI:10.1016/j.jpowsour.2010.12.071.
4. Zheng K, Świerczek K, Bratek J, Klimkowicz A. Cation-ordered perovskite-type anode and cathode materials for solid oxide fuel cells. *Solid State Ionics.* 2014;262:354–8. DOI:10.1016/j.ssi.2013.11.009.
5. Pelosato R, Donazzi A, Dotelli G, Cinzia C, Sora IN, Mariani MP. Electrical characterization of co-precipitated $LaBaCo_2O_{5+\delta}$ and $YBaCo_2O_{5+\delta}$ oxides. *J Europ Ceram Soc.* 2014;34:4257-72. DOI:10.1016/j.jeurceramsoc.2014.07.005.
6. Zhang Y, Yu B, Lü S, Meng X, Zhao X, Ji Y. Effect of Cu doping on $YBaCo_2O_{5+\delta}$ as cathode for intermediate-temperature solid oxide fuel cells. *Electrochim Acta.* 2014;134:107-15. DOI:10.1016/j.electacta.2014.04.126.
7. Yi L.$YBaCo_2O_{5+\delta}$ as a new cathode material for zirconia-based solid oxide fuel cells. *J Alloys Compd.* 2009;477:860-2. DOI:10.1016/j.jallcom.2008.11.010.
8. Kim JH, Manthiram A. $LnBaCo_2O_{5+\delta}$ oxides as cathodes for intermediate-temperature solid oxide fuel cells. *J Electrochem Soc.* 2008;155(4):B385-90. doi:10.1149/1.2839028.
9. Meng F, Xia T, Wang J, Shi Z, Lian J, Zhao H, Bassat JM, Grenier JC. Evaluation of layered perovskites $YBa_{1-x}Sr_xCo_2O_{5+\delta}$ as cathodes for intermediate temperature solid oxide fuel cells. *Int J Hydrogen Energy.* 2014;39:4531-43. DOI:10.1016/j.ijhydene.2014.01.008.
10. Zhang X, Hao H, He Q, Hu X. High-temperature electronic transport properties of Fe-doped $YBaCo_2O_{5+\delta}$. *Phys B.* 2007;39(1):118-21. DOI:10.1016/j.physb.2007.02.027.
11. Zhang K, Ge L, Ran R, Shao Z, Liu S. Synthesis, characterization and evaluation of cation-ordered $LnBaCo_2O_{5+\delta}$ as materials of oxygen permeation membranes

and cathodes of SOFCs. *Acta Mater.* 2008;56(17):4876-89. DOI:10.1016/j.actamat.2008.06.004.
12. Kim JH, Kim YN, Bi Z, Manthiram A, Paranthaman MP, Huq A. Overcoming phase instability of $RBaCo_2O_{5+\delta}$ (R= Y and Ho) by Sr substitution for application as cathodes in solid oxide fuel cells. *Solid State Ionics.* 2013;253:81-7. DOI:10.1016/j.ssi.2013.09.001.
13. Sednev AL, Zuev AYu, Tsvetkov DS. Oxygen content and thermodynamic stability of $YBaCo_2O_{6-\delta}$ double perovskite. *Adv Mater Sci Eng*. Forthcoming 2017.
14. Xuening J, Hongxia X, Qian W, Lei J, Xiangnan L, Qiuli X, Yuchao S, Qingyu Z. Fabrication of $GdBaCo_2O_{5+d}$ cathode using electrospun composite nanofibers and its improved electrochemical performance. *J Alloys Compd.* 2013;557:184-9. DOI:10.1016/j.jallcom.2013.01.015.
15. Buassi-Monroy OS, Luhrs CC, Chávez-Chávez A, Michel CR. Synthesis of crystalline $YCoO_3$ perovskite via sol–gel method. *Mater Lett.* 2004;58(5):716-8. DOI:10.1016/j.matlet.2003.07.001.
16. Urusova AS, Cherepanov VA, Aksenova TV, Gavrilova LY, Kiselev EA. Phase equilibria, crystal structure and oxygen content of intermediate phases in the Y–Ba–Co–O system. *J Solid State Chem*. 2013;202:207-14. DOI:10.1016/j.jssc.2013.03.037.
17. Knizek K, Jirak Z, Hejtmanek J, Veverka M, Marysko M, Hauback BC, Fjellvag H. Structure and physical properties of $YCoO_{3-\delta}$ at temperatures up to 1000 K. *Phys Rev B: Condens Matter.* 2006;73:214443. DOI:10.1103/PhysRevB.73.214443.
18. Balamurugan S, Takayama-Muromachi E. Structural and magnetic properties of high-pressure/high-temperature synthesized $(Sr_{1-x}R_x)CoO_3$ (R=Y and Ho) perovskites. *J Solid State Chem.* 2006;179(7):2231-6. DOI:10.1016/j.jssc.2006.04.028.
19. Felser C, Yamaura K, Cava RJ. The electronic structure of hexagonal BaCoO3. *J Solid State Chem.* 1999;146(2):411-7. DOI:10.1006/jssc.1999.8382.
20. Botta PM, Pardo V, de la Calle C, Baldomir D, Alonso JA, Rivas J. Ferromagnetic clusters in polycrystalline $BaCoO_3$. *J Magn Magn Mater.* 2007;316(2):e670-3. DOI:10.1016/j.jmmm.2007.03.058.
21. Jacobson AJ, Hutchinson JL. An investigation of the structure of 12H $BaCoO_{2.6}$ by electron microscopy and powder neutron diffraction. *J Solid State Chem.* 1980;35(3):334-40. DOI:10.1016/0022-4596(80)90530-7.
22. Demazeau G, Pouchard M, Hagenmuller P. Sur de nouveaux composés oxygénés du cobalt+ III dérivés de la perovskite. *J Solid State Chem.* 1974;9(3):202-9. DOI:10.1016/0022-4596(74)90075-9.
23. Feng G, Xue Y, Shen H, Feng S, Li L, Zhou J, Yang H, Xu D. Sol–gel synthesis, solid sintering, and thermal stability of single-phase $YCoO_3$. *Phys Status Solidi A*. 2012;209(7):1219-24. DOI:10.1002/pssa.201127710.
24. Kropanev AYu, Petrov AN. Termicheskie svoystva cobal'titov redkozemel'nykh elementov sostava $RCoO_3$ [Termal properties of cobaltites of rare earth elements $RCoO_3$]. *Zhurnal Fizicheskoy Khimii.* 1984;58(1):50-3. Russian.

25. Kropanev AYu, Petrov AN. Termicheskaya ustoychivosť cobal'titov $LnCoO_3$ na vozduhe (Ln – Sm, Eu, Gs, Tb, Dy, Ho) [termal stability of cobaltites $LnCoO_3$ in air]. *Izv AN SSSR. Neorganicheskie materialy*. 1983;19(12):2027-30. Russian.
26. Kozlenko DP, Jirák Z, Golosova NO, Savenko BN. Magnetic ground state and the spin-state transitions in YBaCo2O5.5. *Eur Phys J B*. 2009;70(3):327-34. DOI:10.1140/epjb/e2009-00228-x.
27. Aurelio G, Curiale J, Sánchez RD, Cuello GJ. Probing phase coexistence and stabilization of the spin-ordered ferrimagnetic state by calcium addition in the $Y(Ba_{1-x}Ca_x)Co_2O_{5.5}$ layered cobaltites using neutron diffraction. *Phys Rev B*. 2007;76(21):214417. DOI:10.1103/PhysRevB.76.214417.

Cite this article as:
Sednev AL, Tsvetkov DS. Study and optimization of the synthesis routine of the single phase $YBaCo_2O_{6-\delta}$ double perovskite. *Chimica Techno Acta*. 2017;4(3):183–90. DOI:10.15826/chimtech/2017.4.3.03.

DOI: 10.15826/chimtech/2017.4.3.04

Soliev L., Dzhumaev M. T., Dzhabborov B. B.
Chimica Techno Acta. 2017. Vol. 4, No. 3. P. 191–201.
ISSN 2409–5613

L. Soliev[1], M.T. Dzhumaev[2], B.B. Dzhabborov

Tajik State Pedagogical University named after S. Ayni
121 Prospect Rudaki, Dushanbe, 734003, Tajikistan
[1]e-mail: Soliev.lutfullo@yandex.com
[2]e-mail: Jumaev_m@bk.ru

Solubility and phase equilibria in the Na, Ca || CO_3, HCO_3–H_2O system at 0 °C

The information on phase equilibria in the Na,Ca || CO_3, HCO_3-H_2O system at 0 °C, predicted earlier by the translation method, has been obtained experimentally. Dependences of the concentration parameters reflecting phase equilibria are presented in the form of geometric patterns on the solubility diagram for the system studied. The diagram of solubility of the investigated system at 0 °C is constructed for the first time, in which the contours of the crystallization fields of individual phases are outlined, the conditions for their co-crystallization in the form of curves and points are determined.

Keywords: solubility; phase equilibria; liquid phase; chemical analysis; crystallo-optical analysis; phase diagram.

Received: 05.10.2017; accepted: 16.10.2017; published: 20.10.2017.

Л. Солиев[1], М.Т. Джумаев[2], Б.Б. Джабборов

Таджикский государственный педагогический
университет им. С. Айни,
пр-т Рудаки, 121, 734003, Душанбе, Таджикистан
[1]e-mail: Soliev.lutfullo@yandex.com
[2]e-mail: Jumaev_m@bk.ru

Растворимость и фазовые равновесия в системе Na, Ca || CO_3, HCO_3–H_2O при 0 °C

Экспериментальным путем получены сведения о фазовых равновесиях в системе Na,Ca || CO_3, HCO_3-H_2O при 0 °C, прогнозированные ранее методом трансляции. Параметры концентрационных зависимостей, отражающие фазовые равновесия, представлены в виде геометрических образов исследованной системы. Впервые построена диаграмма растворимости исследованной системы при 0 °C, в которой очерчены контуры полей кристаллизации отдельных фаз, определены условия их совместной кристаллизации в виде кривых и точек.

Ключевые слова: растворимость; равновесие; жидкая фаза; химический анализ; кристаллооптический анализ; диаграмма; геометрические образы.

Introduction

The studied four-component Na, Ca || CO_3, HCO_3–H_2O system is an integral part of the more complex six-component Na, Ca || SO_4, CO_3, HCO_3, F–H_2O system. The phase diagram of the latter system provides the conditions for the utilization of liquid wastes in the aluminum production. Sewage from the cryolite regeneration departments of aluminum plants contains fluorides, carbonates, hydrogen carbonates and sulfates of sodium and calcium [1, 2]. The processes of salt crystallization and salt dissolution in aqueous solutions of these wastes are determined by the regularities of phase equilibria in the six-component Na, Ca || SO_4, CO_3, HCO_3, F–H_2O system, as well as in five- and four-component its constituent systems.

The present work has aimed to study the solubility in the Na, Ca || CO_3, HCO_3–H_2O system at 0 °C in order to establish the concentration parameters of geometrical images and separation of the crystallization fields of individual equilibrium solids in the phase diagrams. The phase equilibria of the investigated system were established by the translation method earlier [3], and its phase diagram was constructed.

The equilibrium solid phases in the studied system at 0 °C are: calcite $CaCO_3$ denoted further as (Cc); hydrogenated sodium carbonate $Na_2CO_3 \cdot 10H_2O$ denoted further as (C10); geylussite $Na_2CO_3 \cdot CaCO_3 \cdot 5H_2O$ denoted further as (Gl); nahcolit $NaHCO_3$ denoted further as (Nh) and calcium bicarbonate $Ca(HCO_3)_2$ denoted further as (Cbc) [4, 5].

Experimental

Following reagents were used as starting materials: $NaHCO_3$ («chemically pure» grade), Na_2CO_3 («pure» grade); $CaCO_3$ («pure» grade), and $Ca(HCO_3)_2$ («chemically pure» grade). Experiments were performed using so-called «saturation method» [6].

Based on the available reference data [4, 5] the mixtures of precipitates with saturated solutions that corresponded to the non-variant points from the three-component systems: Na_2CO_3–$NaHCO_3$–H_2O; Na_2CO_3–$CaCO_3$–H_2O; $NaHCO_3$–$Ca(HCO_3)_2$–H_2O and $CaCO_3$–$Ca(HCO_3)_2$–H_2O constituting the four-component system under investigation have been prepared first. Then using afore mentioned translation approach [3] that transfers the non-variant points from the three-component section to the four-component section the prepared saturated solutions with the correspondent equilibrium solid precipitates were kept in a thermostat at 0 °C under stirring until equilibration. Thermal stabilization was performed inside a LT-TWC/22 ultra-thermostat. Stirring was performed using a PD-09 magnetic stirrer for 50–120 h. Temperature was maintained with an accuracy of ±0.1 °C using a contact thermometer. The crystallization of solids was monitored with a POLAM-R311 microscope. After equilibrium in the system was achieved, equilibrium solid phases were photographed with a Sony-DSC-S500 digital camera.

A Buchner funnel with an ash-free filter paper (Blue Band) connected to a vacuum pump has been used for separation of the liquid phase and solid phase. The precipitate after filtration was washed with 96 % ethanol and then dried at 120 °C. A chemical analysis of products was performed according to the standard techniques [7–9].

Results and discussion

The results of crystal-optical analysis of equilibrium solid phases (micrographs), employing the method described in [10], are shown in Fig. 1. The results of chemical analysis for the saturated solutions are listed in Table 1.

Based on the obtained result the solubility diagram for the Na, Ca || CO_3, HCO_3–H_2O system at 0°C has been constructed (Fig. 2). The location of non-variant points on the diagram, which are belonging to the three-component section (E_n^3) and to the four-component section (E_n^4), where n – is the point number, were determined by the center of mass method [11].

Fig. 2 represents the general part (*a*) and the salt part (*b*) of the solubility diagram for the Na, Ca || CO_3, HCO_3–H_2O system at 0 °C, illustrating the mutual arrangement and relative sizes of the crystallization fields of the correspondent equilibrium phases.

As can be seen from Fig. 2, the crystallization fields of calcite $CaCO_3$ (Cc) and calcium bicarbonate $Ca(HCO_3)_2$ (CHC) occupy a considerable area in the diagram that indicate low solubility of these salts at the studied condition. A comparison of obtained results for the solubility value in the Na, Ca || CO_3, HCO_3–H_2O system at 0 °C, studied in the present work, and at 25 °C reported earlier [12] shows the general tendency of its decrease with the decrease of temperature.

The description of the geometric images (fields, curves, and points) that have shown in Fig. 2 is listed in Table 2.

Table 1

The solubility values for the nodal (non-variant) points in the Na, Ca || CO_3, HCO_3–H_2O system at 0 °C

Point	The composition of liquid phases, wt %					The phase composition of precipitates
	Na_2CO_3	$NaHCO_3$	$CaCO_3$	$Ca(HCO_3)_2$	H_2O	
e_1	6.570	–	–	–	93.4300	C10
e_2	–	6.490	–	–	93.5100	Nh
e_3	–	–	0.0031	–	99.9969	Cc
e_4	–	–	–	0.144	99.8560	Cbc
E_1^3	5.60	4.610	–	–	89.790	C10 + Nh
E_2^3	12.00	–	0.0048	–	87.9952	C10 + Gl
E_3^3	4.30	–	0.0046	–	95.6954	Gl + Cc
E_4^3	–	4.890	–	0.109	95.001	Nh + Cbc
E_5^3	–	–	0.0014	0.083	99.9156	Cc + Cbc
E_1^4	6.167	2.443	0.0065	–	91.3835	C10 + Nh + Gl
E_2^4	5.904	–	0.0057	0.308	93.7823	Cc + Gl + Cbc
E_3^4	5.510	5.896	–	0.190	88.4040	Nh + Cbc + Gl

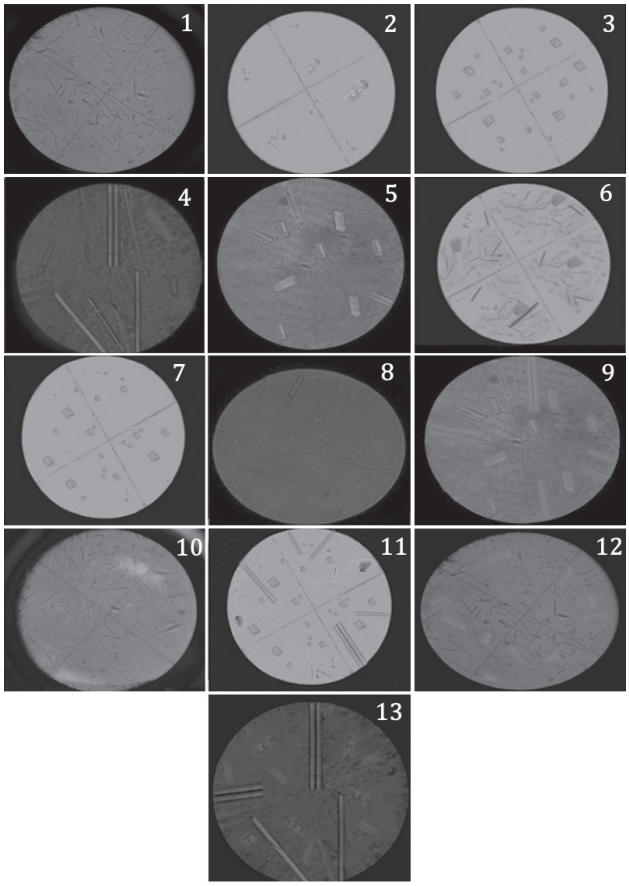

Fig. 1. Micrographs of equilibrium solid phases in the Na, Ca || CO_3, HCO_3–H_2O system at 0 °C: 1 – C10, 2 – Gl, 3 – Cc, 4 – Cbc, 5 – Nh, 6 – C10 + Gl, 7 – Gl + Cc, 8 – Cc + Cbc, 9 – Cbc + Nh, 10 – C10 + Nh, 11 – Cc + Gl + Cbc , 12 – C10 + Gl + Nh, 13 – Nh + Gl + Cbc

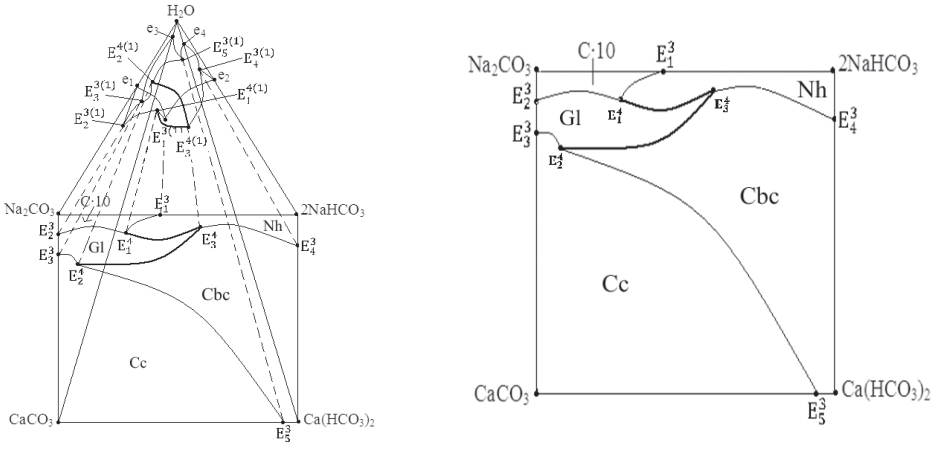

Fig. 2. Solubility diagram for the Na, Ca || CO_3, HCO_3–H_2O system at 0 °C: (*a*) general part and (*b*) salt part

Table 2

Description of the geometric images contents in Fig. 2

Notation of the geometric images	Content
e_1	Solubility of sodium carbonate in water
e_2	Solubility of sodium bicarbonate in water
e_3	Solubility of calcium carbonate in water
e_4	Solubility of calcium bicarbonate in water
E_1^3	Co-crystallization point for C10 + Nh in the Na_2CO_3–$NaHCO_3$–H_2O system
E_2^3	Co-crystallization point for C10 + Gl in the Na_2CO_3–$CaCO_3$–H_2O system
E_3^3	Co-crystallization point for Gl + Cc in the Na_2CO_3– $CaCO_3$–H_2O system
E_4^3	Co-crystallization point for Nh + Cbc in the $NaHCO_3$–$Ca(HCO_3)_2$–H_2O system
E_5^3	Co-crystallization point for Cc + Cbc in the $CaCO_3$–$Ca(HCO_3)_2$–H_2O system
E_1^4	Co-crystallization point for Nh + C10 + Gl in the Na, Ca || CO_3, HCO_3–H_2O system
E_2^4	Co-crystallization point for Gl + Cc + Cbc in the Na, Ca || CO_3, HCO3–H_2O system
E_3^4	Co-crystallization point for Gl+Cbc+Nh in the Na, Ca || CO_3, HCO_3–H_2O system
$E_1^3 - E_1^4$	Co-crystallization curve for C10 + Nh in the Na_2CO_3–$NaHCO_3$–H_2O system
$E_2^3 - E_1^4$	Co-crystallization curve for C10 + Gl in the Na2CO3–CaCO3–H2O system
$E_3^3 - E_2^4$	Co-crystallization curve for Cc + Gl in the Na2CO3–$CaCO_3$–H_2O system
$E_4^3 - E_3^4$	Co-crystallization curve for Cbc + Nh in the $NaHCO_3$–$Ca(HCO_3)_2$–H_2O system
$E_5^3 - E_2^4$	Co-crystallization curve for Cc + Cbc in the $CaCO_3$–$Ca(HCO_3)_2$–H_2O system
$E_1^3\,Na_2CO_3\,E_2^3E_1^4E_1^3$	C10 crystallization field
$E_1^3\,NaHCO_3\,E_4^3E_3^4E_1^4E_1^3$	Nh crystallization field
$E_2^3E_1^4E_3^4E_2^4E_3^3E_2^3$	Gl crystallization field
$E_3^3\,CaCO_3\,E_5^3E_2^4E_3^3$	Cc crystallization field
$E_5^3E_2^4E_3^4E_4^3\,Ca(HCO_3)_2\,E_5^3$	Cbc crystallization field

Введение

Исследуемая четырехкомпонентная система Na, Ca || CO_3, HCO_3–H_2O является составной частью более сложной шестикомпонентной системы Na, Ca || SO_4, CO_3, HCO_3, F–H_2O состояния фазовых равновесий, в которой определяют условия утилизации жидких отходов алюминиевого производства. Сточные воды отделений регенерации криолита алюминиевых заводов содержат фториды, карбонаты, гидрокарбонаты и сульфаты натрия и кальция [1–2]. Процессы кристаллизации и растворения солей в водных растворах этих отходов определяются закономерностями фазовых равновесий в шестикомпонентной системе Na, Ca || SO_4, CO_3, HCO_3, F–H_2O, составляющих ее пяти – и четырехкомпонентных систем.

В настоящей работе рассмотрены результаты исследования системы Na, Ca || CO_3, HCO_3–H_2O при 0 °С методом растворимости с целью установления концентрационных параметров положения ее геометрических образов и соотношения полей кристаллизации индивидуальных равновесных твердых фаз. Ранее [3] методом трансляции были установлены фазовые равновесия исследуемой системы и построена ее фазовая диаграмма.

Равновесными твердыми фазами исследуемой системы при 0 °С являются: $CaCO_3$ – кальцит (Сц); $Na_2CO_3 \cdot 10H_2O$ – С·10; $Na_2CO_3 \cdot CaCO_3 \cdot 5H_2O$ – гейлюссит (Гл); $NaHCO_3$ – нахколит (Нх) и $Ca(HCO_3)_2$ – кальций гидрокарбонат (СаГ) [4, 5].

Экспериментальная часть

Для опытов были использованы следующие реактивы: $NaHCO_3$ (х. ч.); Na_2CO_3 (ч); $CaCO_3$ (ч); $Ca(HCO_3)_2$ (х. ч.). Опыты проводили по следующей схеме согласно методу донасыщения [6].

Исходя из данных литературы [4, 5], нами предварительно были приготовлены смеси осадков с насыщенными растворами, соответствующими нонвариантным точкам составляющих исследуемую четырехкомпонентную систему трехкомпонентных систем: Na_2CO_3–$NaHCO_3$–H_2O; Na_2CO_3–$CaCO_3$–H_2O; $NaHCO_3$–$Ca(HCO_3)_2$–H_2O и $CaCO_3$–$Ca(HCO_3)_2$–H_2O. Затем, исходя из схемы трансляции нонвариантных точек уровня трехкомпонентного состава на уровень четырехкомпонентного состава [3], приготовленные насыщенные растворы, с соответствующими равновесными твердыми фазами, перемешивая термостатировали при 0 °С до достижения равновесия.

Термостатирование проводили в ультратермостате LT-TWC/22. Перемешивание смеси осуществляли с помощью магнитной мешалки PD-09 в течение 50–120 ч. Температура поддерживалась с точностью ±0,1 °С с помощью контактного термометра. За кристаллизацией твердых фаз наблюдали с помощью микроскопа «ПОЛАМ-Р 311». После достижения равновесия в системе равновесные твёрдые фазы сфотографировали цифровым фотоаппаратом

«SONY-DSC-S500». Достижение равновесия устанавливалось по неизменности фазового состава осадков. Отделение жидкой и твердой фаз осуществляли с помощью вакуумного насоса через обеззоленную (синяя лента) фильтровальную бумагу на воронке Бюхнера. Осадок после фильтрации промывали 96 %-м этиловым спиртом и высушивали при 120 °С. Химический анализ продуктов проводили по известным методикам [7–9].

Результаты и обсуждение

Результаты кристаллооптического анализа [10] равновесных твердых фаз (микрофотографии) представлены на рис. 1, а результаты химического анализа насыщенных растворов приведены в табл. 1.

На основании полученных данных построена диаграмма растворимости системы Na, Ca || CO_3, HCO_3–H_2O при 0 °С, которая представлена на рис. 2. Положение нонвариантных точек уровня трехкомпонентного (E^3_n)

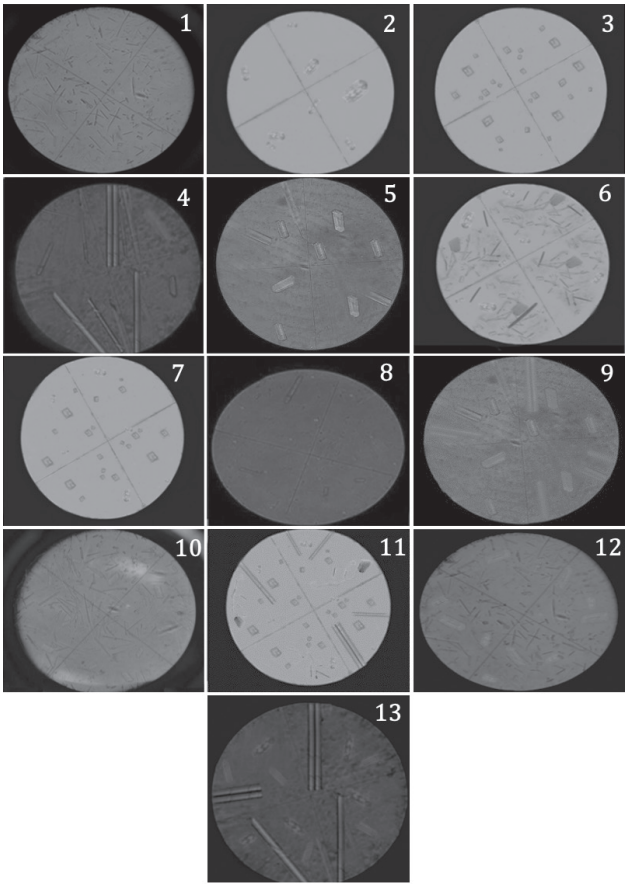

Рис. 1. Микрофотографии равновесных твердых фаз системы Na, Ca || CO_3, HCO_3–H_2O при 0 °С: 1 – C10; 2 – Gl, 3 – Cc; 4 – Cbc; 5 – Nh; 6 – C10 + Gl; 7 – Gl + Cc; 8 – Cc + Cbc; 9 – Cbc + Nh; 10 – C10 + Nh; 11 – Cc + Gl + Cbc; 12 – C10 + Gl + Nh; 13 – Nh + Gl + Cbc

Таблица 1

Растворимость в узловых (нонвариантных) точках системы
Na, Ca || CO_3, HCO_3–H_2O при 0 °C

№ точек	Состав жидкой фазы, мас. %					Фазовый состав осадков
	Na_2CO_3	$NaHCO_3$	$CaCO_3$	$Ca(HCO_3)_2$	H_2O	
e_1	6,570	–	–	–	93,4300	Нх
e_2	–	6,490	–	–	93,5100	Сц
e_3	–	–	0,0031	–	99,9969	СаГ
e_4	–	–	–	0,144	99,8560	С·10 + Нх
E_1^3	5,60	4,610	–	–	89,790	С·10 + Гл
E_2^3	12,00	–	0,0048	–	87,9952	Гл + Сц
E_3^3	4,30	–	0,0046	–	95,6954	Нх + СаГ
E_4^3	–	4,890	–	0,109	95,001	Сц + СаГ
E_5^3	–	–	0,0014	0,083	99,9156	С·10 + Нх + Гл
E_1^4	6,167	2,443	0,0065	–	91,3835	Сц + Гл + СаГ
E_2^4	5,904	–	0,0057	0,308	93,7823	Нх + СаГ + Гл
E_3^4	5,510	5,896	–	0,190	88,4040	Nh + Cbc + Gl

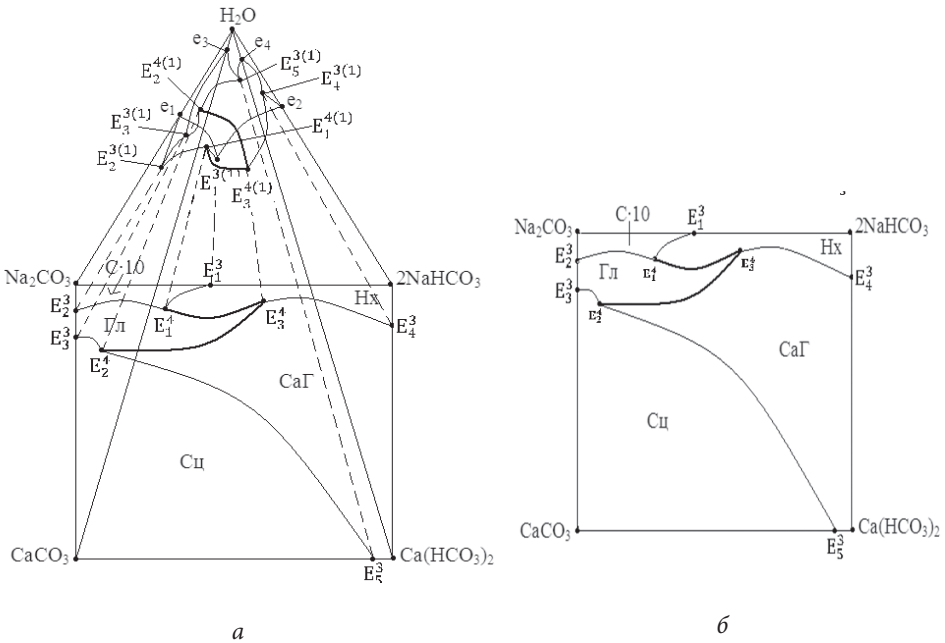

а *б*

Рис. 2. Диаграмма растворимости системы Na, Ca || CO_3, HCO_3–H_2O при 0 °C:
а – общая; *б* – солевая часть

Таблица 2

Описание содержания геометрических образов на рис. 2

Обозначение геометрических образов	Содержание
e_1	Растворимость карбоната натрия в воде
e_2	Растворимость гидрокарбоната натрия в воде
e_3	Растворимость карбонатакальция в воде
e_4	Растворимость гидрокарбоната кальция в воде
E_1^3	Точка совместной кристаллизации С·10 + Нх в системе $Na_2CO3–NaHCO_3–H_2O$
E_2^3	Точка совместной кристаллизации С·10 + Гл в системе $Na_2CO3–CaCO_3–H_2O$
E_3^3	Точка совместной кристаллизации Гл + Сц в системе $Na_2CO_3–CaCO_3–H_2O$
E_4^3	Точка совместной кристаллизации Нх + СаГ в системе $NaHCO_3–Ca(HCO_3)_2–H_2O$
E_5^3	Точка совместной кристаллизации Сц + СаГ в системе $CaCO_3–Ca(HCO_3)_2–H_2O$
E_1^4	Точка совместной кристаллизации Нх + С·10 + Гл в системе Na, Ca || CO_3, $HCO_3–H_2O$
E_2^4	Точка совместной кристаллизации Гл + Сц + СаГ в системе Na, Ca || CO_3, $HCO_3–H_2O$
E_3^4	Точка совместной кристаллизации Гл+СаГ+Нх в системе Na, Ca || CO_3, $HCO_3–H_2O$
$E_1^3 – E_1^4$	Кривая совместной кристаллизации С·10 + Нх в системе $Na_2CO_3–NaHCO_3–H_2O$
$E_2^3 – E_1^4$	Кривая совместной кристаллизации С·10 + Гл в системе $Na_2CO_3–CaCO_3–H_2O$
$E_3^3 – E_2^4$	Кривая совместной кристаллизации Сц + Гл в системе $Na_2CO_3–CaCO_3–H_2O$
$E_4^3 – E_3^4$	Кривая совместной кристаллизации СаГ + Нх в системе $NaHCO_3–Ca(HCO_3)_2–H_2O$
$E_5^3 – E_2^4$	Кривая совместной кристаллизации Сц + СаГ в системе $CaCO_3–Ca(HCO_3)_2–H_2O$
$E_1^3\,Na_2CO_3\,E_2^3E_1^4E_1^3$	Поле кристаллизации С·10
$E_1^3\,NaHCO_3\,E_4^3E_3^4E_1^4E_1^3$	Поле кристаллизации Нх
$E_2^3E_1^4E_3^4E_2^4E_3^3E_2^3$	Поле кристаллизации Гл
$E_3^3\,CaCO_3\,E_5^3E_2^4E_3^3$	Поле кристаллизации Сц
$E_5^3E_2^4E_3^4E_4^3\,Ca(HCO_3)_2\,E_5^3$	Поле кристаллизации СаГ

и четырехкомпонентного (E_n^4) составов, где *n* – номера точек, на диаграмме установлены по массцентрическому методу [11].

На рис. 2 приведена «общая» (*а*) и «солевая» (*б*) части диаграммы растворимости системы Na, Ca || CO_3, HCO_3–H_2O при 0 °С, где отражены взаимное расположение и относительные размеры полей кристаллизации соответствующих равновесных фаз. Как следует из рис. 2, при 0 °С в исследуемой четырехкомпонентной системе поле кристаллизации Сц ($CaCO_3$) и кальций гидрокарбонат СаГ ($Ca(HCO_3)_2$) занимает ее значительную часть, что характеризует малую растворимость данной соли в приведенных условиях. Сопоставление полученных результатов по исследованию растворимости в системе Na, Ca || CO_3, HCO_3–H_2O при 0 °С и при 25 °С [12] в целом указывает на общую тенденцию уменьшения данного показателя с понижением температуры.

Описание содержания геометрических образов (поля, кривые, точки) рис. 2 приведены в табл. 2.

References

1. Morozova VA, Rzhechitskii EP. [Solubility in the NaF – Na_2SO_4 – $NaHCO_3$ – H_2O system at 0 °C]. *Zhurnal Prikladnoi Khimii [Journal of Applied Chemistry*]. 1976;49(5):1152–4. Russian.
2. Morozova VA, Rzhechitskii EP. [Solubility in the systems NaF – $NaNCO_3$ – H_2O, NaF – Na_2SO_3 – H_2O and NaF –Na_2CO_3 – H_2O at 0 °C]. *Zhurnal Neorganicheskoi Khimii* [*Russ J Inorg Chem*]. 1977;22(3):873–4. Russian.
3. Dzhumaev MT, Soliev L, Avloev ShKh, Ikbol G. Phase balance in the Na, Ca // CO_3, HCO_3 – H_2O System at 0 °C. *Vestnik Tadjikckogo natsional'nogo universiteta* (*seriya estesvennikh nauk*) [*Bulletin of the Tajik National University* (*series of natural sciences*)]. 2013;1/1(102):153–6. Russian.
4. Spravochnik eksperimental'nykh dannykh po rastvorimosti mnogokomponentnykh vodno-solevykh system [Reference book on experimental data for solubility in multicomponent water-salt systems]. Vol. 1. Saint-Petersburg: Khimizdat, 2003. 1151 p. Russian.
5. Spravochnik eksperimental'nykh dannykh po rastvorimosti mnogokomponentnykh vodno-solevykh system [Reference book on experimental data for solubility in multicomponent water-salt systems]. Vol. II, Books. 1–2. Saint-Petersburg: Khimizdat, 2004. 1247 p. Russian.
6. Goroshchenko YaG, Soliev L, Gornikov Yu I. Opredelenie polozheniya nonvariantnykh tochek na diagrammakh rastvorimosti metodom donasyshcheniya [Determination of the invariant points' positions on solubility diagrams using the presaturation method]. *Ukrainskii Khimicheskii Zhurnal* [*Ukrainian Journal of Chemistry*]. 1987;53(6):568–71. Russian.
7. Kreshkov AP. Osnovy analiticheskoy khimii [Basics of Analytical Chemistry]. Vol. 2. Leningrad (USSR): Khimiya, 1970. 456 p. Russian.
8. Knipovich YuN, Morachevskii YuV, editors. Analiz mineral'nogo syr'ya [Analysis of mineral raw materials]. Leningrad: Goskhimizdat, 1959. 947 p. Russian.

9. Reznikov AA, Mulikovskaya EP, Sokolov IYu. Metody analiza prirodnykh vod [Methods of natural water analysis]. Moscow: Nedra, 1970. 488 p. Russian.
10. Tatarskii VB. Kristallooptika i immersionnyy metod analiza veshchestv [Crystal Optics and Immersion Method of Substances Analysis]. Leningrad (USSR): Izdatel'stvo LGU, 1948. 268 p. Russian.
11. Goroshchenko Ya G. Masstsentricheskiy metod izobrazheniya mnogokomponentnykh system [The Center of Mass Method for Multi-component Systems Imaging]. Kiev: Naukova Dumka, 1982. 264 p. Russian.
12. Dzhumaev MT, Soliev L, Dzhabborov BB, Ikbol G. Solubility in the Na, Ca || CO_3, HCO_3 – H_2O System at 25°C. *Russ J Inorg Chem.* 2017;62(9):1245–51. DOI:10.1134/S0036023617090169.

Cite this article as:
Soliev L, Dzhumaev MT, Dzhabborov BB. Solubility and phase equilibria in the Na, Ca || CO_3, HCO_3–H_2O system at 0 °C. Chimica Techno Acta. 2017;4(3):191–201. DOI:10.15826/chimtech/2017.4.3.04.

Krylov A.A., Emelyanova Yu.V., Buyanova E.S.,
Morozova M.V., Vylkov A.I., Chuykin A.Yu.
Chimica Techno Acta. 2017. Vol. 4, No. 3. P. 202–208.
ISSN 2409–5613

DOI: 10.15826/chimtech/2017.4.3.05

A.A. Krylov[1], Yu.V. Emelyanova[1], E.S. Buyanova[1], M.V. Morozova[1], A.I. Vylkov[2], A.Yu. Chuykin[2]

[1]Ural Federal University
19 Mira St., 620000, Ekaterinburg, Russia
[2]Institute of High Temperature Electrochemistry UB RAS
20 Akademicheskaya St, 620137, Ekaterinburg, Russia

Materials based on BIFEVOX and bismuth or iron simple oxides nanopowders

Compositions of composite materials based on BIFEVOX and nanopowders of bismuth and iron oxides have been obtained. The absence of chemical interaction between the components has been proved, the total electrical conductivity of materials in the average temperature region has been determined. It has been shown that under the selected formation conditions, it has not yet been possible to achieve significant improvement of the functional characteristics of heterogeneous compositions in comparison with individual phases. However positive results on chemical and structural stability give way to further investigations.

Keywords: BIMEVOX; Oxygen-ion conductors; Electrical conductivity; Impedance spectroscopy.

Received: 22.09.2017; accepted: 17.10.2017; published: 20.10.2017.

Introduction

The family of solid electrolytes with the general formula $Bi_4V_{2-x}Fe_xO_{11-\delta}$ (BIFEVOX) is characterized by high oxygen-ion conductivity at intermediate temperatures 550–950 K [1–5]. The high-temperature γ-modification of the BIFEVOX solid solutions with tetragonal structure (space group *I*4/*mmm*) is obtained at $0.3 \le x \le 0.5$ iron concentration range. For this modification, the electrical conductivity versus temperature dependence is linear, and the activation energy at high temperatures has a value of 0.2–0.4 eV, which is characteristic of BIFEVOX. The transition to an ordered γ′ modification with decreasing temperature is accompanied by a small change of slope of the lg σ – $10^3/T$ dependence and, accordingly, an increase in the activation energy to 0.5–0.7 eV. The tetragonal γ-modification of the $Bi_4V_{2-x}Fe_xO_{11-\delta}$ is sufficiently stable in a wide range of thermodynamic parameters (T = 298 – 1073 K, $\lg pO_2$ (atm) = –0.68 to –18.0) [4, 5]. The change of the structure into the orthorhombic one occurs in atmosphere with low oxygen content ($\lg pO_2$ (atm) <–14.0) at temperatures above 773 K. However, decomposition of the sample does not occur. Evaluation of the structural and thermal stability of BIFEVOX in air at long time exposures (at least two weeks at the same temperature)

in the temperature range 723–1083 K revealed no changes in the structure or appearance of any additional phases [6].

In the last decade composite electrolytes are actively studied as alternative electrolyte materials. It has been shown that in this way it is possible to improve the quality of the material and remove some disadvantages of individual electrolytes [7]. There are examples of creating composite materials with BIMEVOX as their components [8–11]. For the modification of BIFEVOX based electrolyte materials, the approach using simple oxides nanopowders is used in this paper.

Experimental

Samples of $Bi_4V_{2-x}Fe_xO_{11-\delta}$ (x = 0.3, 0.5) solid solutions were synthesized according to the standard ceramic technology [2]. The preparation of nanopowders of bismuth and iron oxides was carried out by laser evaporation of a target and condensation of vapors in a working gas stream at the Institute of Electrophysics of the Ural Branch of the Russian Academy of Sciences. In this method a fiber ytterbium laser LS-1 with diode pumping was used. The average radiation power was 1000 W with a smooth adjustment from 20 to 100 %, the wavelength 1070 nm, and the radiation regime continuous or modulated. The evaporation targets were prepared by pressing from a coarse-grained oxide powder followed by annealing at a temperature providing a partial sintering of the powder to provide mechanical strength of the compact. Composites were prepared by mechanically mixing of the corresponding powders with a simple oxide content of 10 to 50 wt.%. The powders were pressed into pellets with a diameter of 10 mm on a hydraulic press in the form of pellets and annealed at 1073 K.

The phase composition of the final solid oxide products was checked by X-ray powder diffraction (DRON-3 diffractometer, CuKα radiation, pyrolytic carbon monochromator, reflected beam). The particle size of the powders was determined using a laser dispersion analyzer SALD-7101 Shimadzu. The morphology of the obtained powders and their chemical composition were studied using a JEOL JSM6390 LA scanning electron microscope equipped with a JED-2300 energy dispersive X-ray detector. Thermal dilatometric analysis was performed on a DIL 402 C Netzsch dilatometer equipped with a vacuum furnace. Electrical conductivity measurements of the ceramic samples were performed on Elins Z-3000 impedance spectrometer in the temperature range 1073–473 K.

Results and discussion

1. Synthesis and characterization of the materials

$Bi_4V_{2-x}Fe_xO_{11-\delta}$ (x = 0.3, 0.5) samples, obtained by the standard ceramic technology, are single-phase and have the structure of high-temperature tetragonal γ-modification (space group *I*4/*mmm*). The average particle size of $Bi_4V_{2-x}Fe_xO_{11-\delta}$ is in the range of 0.5–10 μm. The bismuth oxide nanopowder is single-phase, and is β-Bi_2O_3 with tetragonal structure. Iron oxide nanopowder contains three crystalline phases where iron is in different oxidation states, so its composition is denoted as FeO_x. This is composed of Fe_3O_4 (magnetite) with its content 69 %, Fe_2O_3

(hematite, 10 %) and ε-Fe_2O_3 (21 %). The average particle size of nanopowders is in the range of 50–100 nm.

In accordance with the results of the XRD, the calculation of the unit cell parameters was carried out for β-Bi_2O_3 in the tetragonal structure (space group *I*4/*mmm*), for Fe_3O_4 in cubic (*Fd*-3*m*), Fe_2O_3 for rhombohedral (space group *R*-3*c*), ε-Fe_2O_3 for orthorhombic (space group *Pna*21) structure. The results are shown in Table 1.

Table 1

Crystal structure parameters of the materials

Composition	*a* ± 0.001, Å	*b* ± 0.001, Å	*c* ± 0.004, Å
$Bi_4V_{1.7}Fe_{0.3}O_{11-\delta}$	3.919	3.919	15.468
$Bi_4V_{1.5}Fe_{0.5}O_{11-\delta}$	3.918	3.918	15.524
β-Bi_2O_3	7.729	7.729	5.648
Fe_3O_4	8.356	8.356	8.356
Fe_2O_3	5.034	5.034	13.727
ε-Fe_2O_3	5.091	8.804	9.446

Taking into account that the BIMEVOX materials are non-stable in a reducing atmosphere as well as $Bi_4V_{2-x}Fe_xO_{11-\delta}$ undergoes transition from tetragonal structure to orthorhombic one in air at ca. 773 K without decomposition [4, 5] the sample of $Bi_4V_{1.5}Fe_{0.5}O_{11-\delta}$ prepared accordingly was investigated in the reducing atmosphere with $\log(pO_2/atm) < -14.0$ by means of dilatometry equipped with special chamber in order to reveal a possible structure transition. The study was carried out with sequential change of gas atmosphere from air via argon to mixture of argon and hydrogen, and back to air in the heating and cooling cycles. When the sample was found to be heated in air a slight change in the slope of curve 1 at 890 K (see Fig. 1) corresponding to an order-disorder type γ↔γ′ phase transition [12] is observed. However, there is no such transition upon heating in the reducing atmosphere while a γ↔β phase transition is observed at *ca*. 850 K. It is worth noting that final cooling curve recorded in air after reduction-oxidation cycling did not show indication of any transition. The unit cell parameters *a* = 3.919 and *c* = 15.509 Å of the cooled sample were found by XRD to remain practically unchanged as compared to those of $Bi_4V_{1.5}Fe_{0.5}O_{11-\delta}$ before the reduction-oxidation treatment. Aforementioned results indicate obvious-

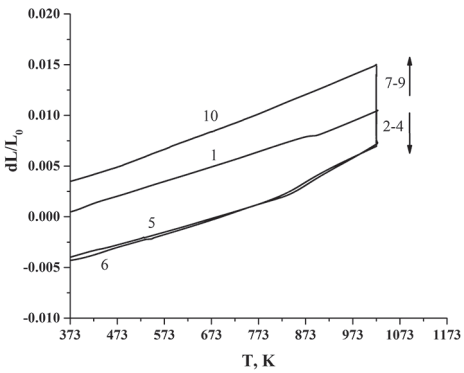

Fig. 1. Thermal strain of the $Bi_4V_{1.5}Fe_{0.5}O_{11-\delta}$ sample: 1 – heating up to 1023 K in air; 2 – 30 minutes holding in air at 1023 K; 3 – 1 hour holding in argon at 1023 K; 4 – 2 hours holding in argon-hydrogen mixture at 1023 K (50 % H_2 and 50 % Ar for this and next three steps); 5 – cooling in argon-hydrogen mixture, 6 – second heating in air-argon mixture; 7 – 30 minutes holding in argon-hydrogen mixture at 1023 K; 8 - 1 hour holding in argon at 1023 K; 9 – 3.5 hours holding in air at 1023 K, 10 – cooling in air

ly in favor of high resistance of the BIFEVOX structure to alteration under reducing conditions. The value of the linear thermal expansion coefficient (LTEC) of the BIFEVOX before and after the oxidation-reduction cycle also did not change significantly and remained in the range 17–19·10^{-6} K^{-1} (Fig. 2). Annealing in hydrogen atmosphere of the $Bi_4V_{1.7}Fe_{0.3}O_{11-\delta}$ sample at 1073 K for 8 hours was carried out to estimate the possibility of decomposition of the $Bi_4V_{2-x}Fe_xO_{11-\delta}$ series at lgPO_2 (atm) <–14.0. In addition to the $Bi_4V_{2-x}Fe_xO_{11-\delta}$ lines, peaks corresponding to $BiVO_4$ and Bi_2O_3 (or solid solutions based on them) as well as to metallic iron were found on the X-ray diffraction pattern of the sample. These results show that samples of the BIFEVOX system, being annealed in air after the reduction, return to their original state with the same crystal structure.

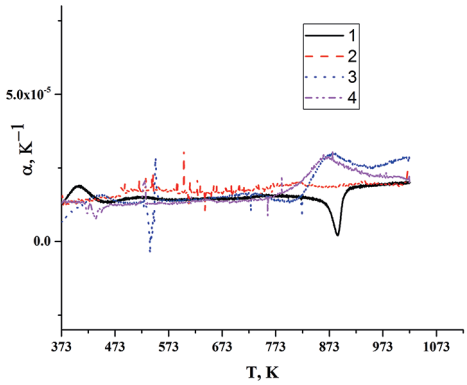

Fig. 2. LTEC change versus temperature: 1 – first heating in air, 2 – cooling in air after reduction-oxidation cycle, 3 – heating in argon-hydrogen mixture, 4 – cooling in argon-hydrogen mixture

2. Preparation and characterization of composite materials.

X-ray phase analysis was used to test the possible interactions in the composite by annealing pellets of $Bi_4V_{1.7(1.5)}Fe_{0.3(0.5)}O_{11-\delta}/x$ wt.%. Bi_2O_3 (FeO_x) composites at 1073 K. All X-ray diffraction patterns contain only composite components lines, without extra reflexes.

As an additional method for determining the phase and element composition of composites, the scanning electron microscopy (SEM) method with the energy-dispersive microanalysis was used. For the sintered samples, the surface and cross-section of the composite pellets were examined. It was established that the surface of the samples is porous, consists of grains of various shapes and sizes, the visual contrast is determined by the topography of the sample surface (Fig. 3).

Large grains of BIFEVOX and fine grains of nanopowder particles are clearly

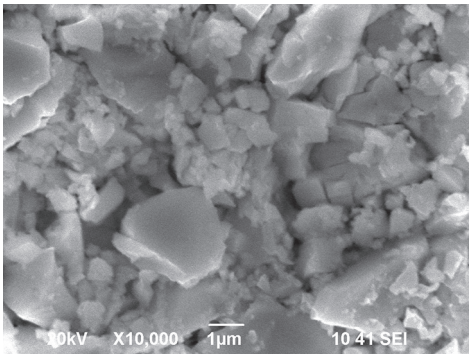

a

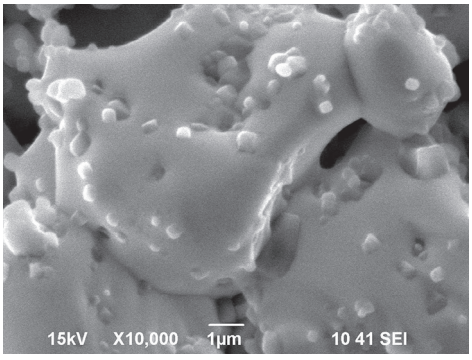

b

Fig. 3. The images of the surface of the composite samples: *a* – $Bi_4V_{1.5}Fe_{0.5}O_{11-\delta}$/40 wt.%. Bi_2O_3; *b* – $Bi_4V_{1.7}Fe_{0.3}O_{11-\delta}$/10 wt.%. FeO_x

visible, the iron oxide particles being aggregated to a lesser extent and covering the coarse grains of the BIMEVOX complex oxide. The particles of bismuth oxide are combined into aggregates and fill the space between the coarse BIMEVOX particles. The chemical composition of the particles was estimated by energy-dispersive X-ray spectroscopy (EDX), and results correspond to the nominal ratio of elements in simple and complex oxides, which additionally indicates the absence of interaction in the composites under the selected processing conditions. An example of the X-ray dispersion energy spectrum of a surface of the $Bi_4V_{1.7}Fe_{0.3}O_{11-\delta}$/10 wt.%. FeO_x composite is shown in Fig. 4.

Determination of the electrochemical characteristics of the composite materials was carried out by the impedance spectroscopy method. Complex plane plots of the BIFEVOX solid solutions consist of two joint half-circles, showing behavior typical for the BIMEVOX family ionic conductors [2].

Fitting of the Cole-Cole plots was performed using the equivalent electrical circuits method [2]. Typical temperature dependences of the total conductivity are

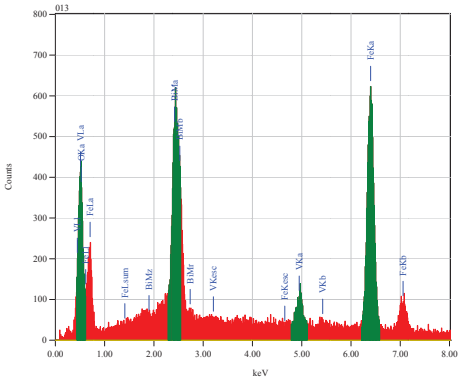

Fig. 4. EDX spectrum of the $Bi_4V_{1.7}Fe_{0.3}O_{11-\delta}$/10 wt.%. FeO_x composite surface

shown in Fig. 5. The dependences of the total conductivity on temperature for the composites studied have the form characteristic for the γ-modification of BIFEVOX. The change of slope is observed in the dependencies at the temperature range 750–850 K. It corresponds to the transition of BIFEVOX to an ordered γ′-modification with decreasing temperature and is accompanied by the increase of the activation energy from 0.4 to 0.7–0.8 eV. The behavior of all lg σ – $10^3/T$ dependencies, corresponding to the composites with different content and nature of the simple oxide added is similar.

As the concentration of the simple oxide increases, the conductivity decreases. This situation is typical for the entire temperature range. This is probably due to an increase in the concentration of the less conducting phase, which are the simple oxides used in comparison with pure BIFEVOX. For example, according to [13, 14], for the β-Bi_2O_3 at 873 K the value of the total electrical conductivity is

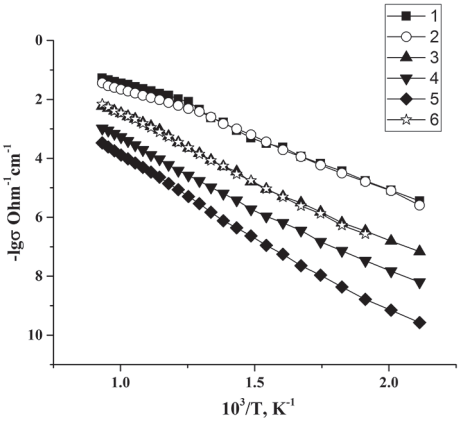

Fig. 5. Total electrical conductivity versus temperature: 1 – $Bi_4V_{1.7}Fe_{0.3}O_{11-\delta}$; 2 – $Bi_4V_{1.5}Fe_{0.5}O_{11-\delta}$; 3 – $Bi_4V_{1.5}Fe_{0.5}O_{11-\delta}$/wt.% FeO_x; 4 – $Bi_4V_{1.5}Fe_{0.5}O_{11-\delta}$/wt.% FeO_x; 5 – $Bi_4V_{1.5}Fe_{0.5}O_{11-\delta}$/40 wt.% Bi_2O_3; 6 – $Bi_4V_{1.7}Fe_{0.3}O_{11-\delta}$/10 wt.% Bi_2O_3

~10^{-3} Ohm^{-1} cm^{-1}, for $Bi_4V_{1.7}Fe_{0.3}O_{11-\delta}$ in our work it is 1.5×10^{-2} Ohm^{-1} cm^{-1}. The effect of an increase of the overall electrical conductivity values of composite samples, which could be associated with a possible increase in the sintering quality of the bars, is not observed.

Conclusions

Thus, compositions of composite materials based on BIFEVOX and nanopowders of bismuth and iron oxides have been obtained, the absence of interaction between them has been proved, the total electrical conductivity of materials in the region of average temperatures has been determined. It has been shown that, under the selected formation conditions, it has not yet been possible to achieve significant improvement of the functional characteristics of heterogeneous compositions in comparison with individual phases. However, the results obtained can serve as a basis for further searching for optimal solutions.

Acknowledgements

The work was partially supported by the Scholarship of the President (SP-3376.2016.1) and Russian Foundation for Basic Research (project No 17-53-04098).

References

1. Garcia-Gonzalez E, Arribas M, Gonzalez-Calbet JM. Short-Range-Long-Range Order Transformation in the $Bi_4V_{2-x}Fe_xO_{11-y}$ Series. *Chem Mater.* 2001;13(1):96–102. DOI:10.1021/cm0003929.
2. Buyanova ES, Petrova SA, Emel'yanova YuV, Blinova AL, Morozova MV, Zhukovskii VM, Zhuravlev VD. Preparation, Structure, and Charge Transport Characteristics of BIFEVOX Ultrafine Powders. *Russ J Inorg Chem.* 2009;54(8):1193–204. DOI: 10.1134/S0036023609080051.
3. Pena V, Rivera A, Leon C, Santamaria J, Garcia-Gonzalez E, Gonzalez-Calbet JM. Correlated Oxygen Diffusion in BIFEVOX. *Chem Mater.* 2002;14(4):1606–9. DOI:10.1021/cm010743z.
4. Zhukovskii VM, Buyanova ES, Emel'yanova YuV, Morozova MV, Shafigina RR, Zakharov RG, Zhuravlev VD. Synthesis, Structure, and Conductivity of BIMEVOX Oxide Ceramics. *Russ J Electrochem.* 2009;45(5):512–9. DOI:10.1134/S1023193509050024.
5. Morozova MV, Buyanova ES, Emelyanova JuV, Zhukovskiy VM, Petrova SA. High-conducting oxide ceramics BIMEVOX: synthesis, structure, properties. *Solid State Ionics.* 2011;192(1):153–7. DOI:10.1016/j.ssi.2010.04.020.
6. Morozova MV, Buyanova ES, Petrova SA, Khisametdinova VV, Emel'yanova YuV, Shatokhina AN, Zhukovskii VM. Structural and Thermal Stability of BIMEVOX Oxygen Semiconductors. *Russ J Electrochem*. 2011;47(4):448–52. DOI:10.1134/S1023193511040100.
7. Rondao AIB, Patrıcio SG, Figueiredo FML, Marques FMB. Composite electrolytes for fuel cells: Long-term stability under variable atmosphere. *Int J Hydrogen Energy.* 2014;39:5460–9. DOI:10.1016/j.ijhydene.2013.12.125.

8. Fuierera P, Maiera M, Exner J, Moos R. Anisotropy and thermal stability of hot-forged BICUTIVOX oxygen ion conducting ceramics. *J Eur Ceram Soc.* 2014;34(4):943–51 DOI:10.1016/j.jeurceramsoc.2013.10.016.
9. Sunarso J, Baumann S, Serra JM, Meulenberg WA, Liu S, Lin YS, Diniz da Costa JC. Mixed ionic-electronic conducting (MIEC) ceramic-based membranes for oxygen separation. *J Membrane Science.* 2008;320(1-2):13–41. DOI: org/10.1016/j.memsci.2008.03.074.
10. Sabolsky EM, Razmyar S, Sabolsky K. Nano-ceria enhancement of $Bi_2Cu_{0.1}V_{0.9}O_{5.35}$ (BICUVOX) ceramic electrolytes. *Mater Lett.* 2012;76:47–50. DOI:10.1016/j.matlet.2012.02.048.
11. Piva RH, Piva DH, Venturini J, Floriano R, Morelli MR. Inhibition of order–disorder phase transition and improvements in the BICUVOX.1 properties by using yttria-stabilized zirconia particles. *Ceram Int.* 2014;41(1):171–7. DOI:10.1016/j.ceramint.2014.08.055.
12. Buyanova ES, Shafigina RR, Morozova MV, Emel'yanova YuV, Khisametdinova VV, Zhukovskii VM, Petrova SA, Tarakina NV. Electrochemical Characteristics, Thermal and Chemical Compatibility in the $La_{0.7}Sr_{0.3}CoO_3$ Electrode-γ-BIFEVOX Electrolyte System. *Russ J Inorg Chem.* 2013;58(5):554–8. DOI:10.1134/S0036023613050033.
13. Sammes NM, Tompsett GA, Näfe H, Aldinger F. Bismuth based oxide electrolytes— structure and ionic conductivity. *J Eur Ceram Soc.* 1999;19(10):1801–26. DOI:10.1016/S0955-2219(99)00009-6.
14. Kharton VV, Marques FMB, Atkinson A. Transport properties of solid oxide electrolyte ceramics: a brief review. *Solid State Ionics.* 2004;174:135–49. DOI:10.1016/j.ssi.2004.06.015.

Cite this article as:
Krylov AA, Emelyanova YuV, Buyanova ES, Morozova MV, Vylkov AI, Chuykin AYu. Materials based on BIFEVOX and bismuth or iron simple oxides nanopowders. *Chimica Techno Acta*. 2017;4(3):202–8. DOI:10.15826/chimtech/2017.4.3.05.

Please note that all new submissions will be accepted in English only. Requirements for the manuscript preparation are available on the Journal's website and in the following template

Chimica Techno Acta manusctipt style guidelines (title)

A.N. Authorname[a], A.N. Authorname[b], A.N. Authorname[ab]
a Institution, address, city, country
b Institution, address, city, country
e-mail: corresponding_author@e-mail.com

Abstract

The abstract should be a single paragraph (up to 300 words) in plain text (that means – no formulae or references are permitted) that summarises the content of the article. It should set the main objectives and results of the work; giving the reader a clear idea of what has been achieved. An abstract should not be extremely short though – if yours is 1–2 sentences long, then you're not doing it right. Make sure that you use well-known, searchable terms and phrases.

Keywords: short; searchable; keywords (up to 10).

Introduction

An introduction should 'set the scene' of the work. It should clearly explain both the nature of the problem under investigation and its background. It should start off general and then focus in to the specific research question you are investigating. Ensure you include all relevant references.

Experimental (if appropiate)

Descriptions of the experiments should be provided in enough detail so that a skilled researcher is able to repeat them. Methods already published or experimental techniques already described elsewhere should be indicated by a reference. Only non-standard apparatus should be described in details; commercially available instruments are referred to by their stock numbers.

Results and discussion

This is undoubtedly the most important section of your article. It should consist of the logically ordered sequence of text, formulae, images and tables.

All formulae which appear in their own line should be numbered:

$$A = B + C \tag{1}$$

Tables should be used only when they can present information more efficiently than running text or even an image:

Table 1

Just an ordinary table without any sophisticated formatting applied

A	B	C	D
1	2	3	4
+	+	+	-

All illustrations should be of a high quality (300 dpi or higher) and should be placed in the flow of the text, not in the end of an article:

Fig. 1. Just an ordinary image

Please bear in mind that all illustrations and tables should fit smoothly within either single column (approx. 6 cm) or double column (approx. 12 cm) width.

Conclusions

Your conclusions should summarize the main paper, underline the interpretation of the key results and highlight the novelty and significance of the work. They may address some plans for relevant future work as well.

Acknowledgements (if appropiate)

All sources of funding such as grants should be declared here. Individuals who contributed to the research but are not co-authors may also be briefly acknowledged.

References

A reference should be indicated in square brackets in line with the text (e.g. [1]). The actual references in the reference list should be numbered in the order in which they appear in the text. In Chimica Techno Acta so-called Vancouver Citation Style is adopted almost as it is described in the following public domain textbook [1]:

1. Patrias K. Citing medicine: the NLM style guide for authors, editors, and publishers [Internet]. 2nd ed. Wendling DL, technical editor. Bethesda (MD): National Library of Medicine (US); 2007- [updated 2015 Oct 2; cited 2017 Jun 07]. Available from: http://www.nlm.nih.gov/citingmedicine

Note that opposed to [1] we omit the date of publication (leaving year only) of the referenced journal article, as almost all journals are continuously paginated throughout the volume. And another one – DOI or a hyperlink should always come last in a reference. These are the only major differences between our style and such described in [1], so when in doubt – you can always refer to [1], it contains tremendous number of well-organized examples.

For your convenience, below are some references to the different types of publications:

Books

2. Livingstone S. The Chemistry of Ruthenium, Rhodium, Palladium, Osmium, Iridium and Platinum. Oxford: Pergamon; 1973. 222 p.

3. Bard AJ, Faulkner LR. Electrochemical Methods: Fundamentals and Applications. 2nd ed. New York: John Wiley & Sons; 2001. 833 p.

Books not in English

4. Evdokimov AA, Efremov VA, Trunov VK, Kleyman IA, Tananaev IV. Soedineniya redkozemel'nykh elementov. Molibdaty, vol'framaty [Rare-earth elements' compounds. Molibdates, wolframates]. Moscow: Nauka; 1991. 267 p. Russian.

* Translation of the title in square brackets is not required, but highly desirable.

* For Cyrillic languages, such as Russian, please use consistent transliteration system.

There are plenty, but we strongly recommend BGN/PCGN Romanization as it's one of the easiest to read and implement (https://en.wikipedia.org/wiki/BGN/PCGN_romanization_of_Russian).

Journal articles

5. Zuev AYu, Tsvetkov DS. Oxygen nonstoichiometry, defect structure and defect-induced expansion of undoped perovskite $LaMnO_{3\pm\delta}$. Solid State Ionics. 2010;81(11–12):557–63. DOI:10.1016/j.ssi.2010.02.024

6. Shannon RD. Revised effective ionic radii and systematic studies of interatomic distances in halides and chalcogenides. Acta Cryst. 1976;A32:751–67. DOI:10.1107/S0567739476001551

7. Allred AL, Rochow EG. A scale of electronegativity based on electrostatic force. J Inorg Nucl Chem. 1958;5(4):264–8. DOI:10.1016/0022-1902(58)80003-2

* For the majority of chemical journals corresponding abbreviation is defined in Chemical Abstracts Service Source Index (CASSI, http://cassi.cas.org). If an abbreviation is not available there, please use the full name of a journal.

* Note that DOI of an article, when available, should always be provided.

Journal articles on the Internet (e.g. for online-only journals without DOI)

8. Tkach V, Nechyporuk V, Yagodynets P. Descripción matemática de la síntesis electroquímica de polímeros conductores en la presencia de surfactants. Avances en Química [Internet]. 2013[cited 2016];8(1):9-15. Spanish. Available from: http://erevistas.saber.ula.ve/index.php/avancesenquimica/article/download/6357/6168

Conference abstracts

9. Zuev AYu, Sereda VV, Malyshkin DA, Ivanov IL, Tsvetkov DS. Mechano-chemical coupling in double perovskites as energy related materials. In: Abstracts of the XX Mendeleev Congress on general and applied chemistry, Vol. 3; 2016 Sep 26-30; Ekaterinburg, Russia. p. 325.

10. Steparuk AS, Usachev SA, Tsvetkov DS, Sosnovskikh VYa, Zuev AYu. Novyy katodnyy material na osnove mayenita dlya elektrokhimicheskogo karboksilirovaniya organicheskikh soedineniy [New mayenite-based cathode material for electrochemical carboxylation of organic compounds]. In: Tezisy dokladov XXVI Rossiyskoy molodezhnoy nauchnoy konferentsii "Problemy teoreticheskoy i eksperimental'noy khimii" [Abstracts of XXVI Russian scientific conference for young scientists "Problems of theoretical and experimental chemistry"]; 2016 Apr 27-29; Ekaterinburg, Russia. p. 285-286. Russian.

Dissertations

11. ten Donkelaar SFP. Development of Stable Oxygen Transport Membranes [dissertation]. Enschede (The Netherlands): University of Twente; 2015. 140 p.

Patents

12. Chemezov OV, Batukhtin VP, Apisarov AP, Isakov AV, Zaikov YuP, inventors; Institute of High-Temperature Electrochemistry UB RAS, assignee. Sposob polucheniya nano- i mikrovolokon kremniya elektrolizom dioksida kremniya iz rasplavov soley. Russian Federation patent RU 2427526. 2011 Aug 27. Russian.

13. Menta E, Da Re G, Grugni M., authors; Cti Europe S.R.L., assignee. Derivatives of chromen-2-one as inhibitors of vegf production in mammalian cells. United States patent US20060122387 A1. 2006 Jun 8.

Учредитель – Уральский федеральный университет имени первого Президента России Б. Н. Ельцина
620002, Россия, Екатеринбург, ул. Мира, 19

Редактор *Е. Е. Крамаревская*
Художник-оформитель *Е. Р. Даурова*
Верстальщик *В. К. Матвеев*

Свидетельство о регистрации
ПИ № ФС77-56172 от 15.11.2013

Адрес журнала:
Россия, 620000,
Екатеринбург, ул. Мира, 28, оф. Х-268
E-mail: t.a.pospelova@urfu.ru

Формат 70×100/16. Заказ № 279.
Тираж 500 экз.

Отпечатано в типографии
Издательско-полиграфического центра УрФУ
620000, Екатеринбург, ул. Тургенева, 4
Тел.: +7 (343) 350-56-64, 350-90-13
Факс: +7 (343) 358-93-06
E-mail: press-urfu@mail.ru

Chimica Techno Acta

Founded by Ural Federal University named after
the first President of Russia B. N. Yeltsin
19, Mira St., Ekaterinburg, 620002, Russia

Journal Registration Certificate
PI № FS 77-56172 as of 15.11.2013

Principal Contact
Office X-268, Mira Str.,
620000, Ekaterinburg, Russia
E-mail: t.a.pospelova@urfu.ru

Format 70×100/16.
Circulation 500 cop.

Publisher – Ural Federal University
Publishing Centre
4, Turgenev St., 620000 Ekaterinburg, Russia
Phone: +7 343 350 56 64, +7 343 350 90 13
Fax: +7 343 358 93 06
E-mail: press-urfu@mail.ru